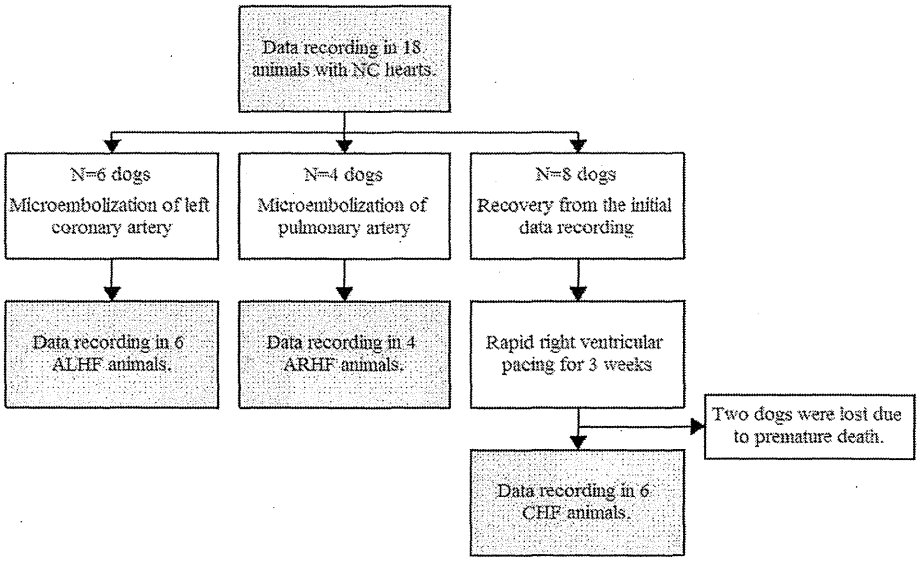

Fig. 1 Study protocol with intervention sequence and cardiac conditions. *NC* normal control, *ALHF* acute left heart failure, *ARHF* acute right heart failure, *CHF* chronic heart failure

connected to a pressure amplifier (AP-610J, Nihon Kohden, Tokyo, Japan), the pressure transducers were balanced at atmospheric pressure, calibrated against a mercury manometer, and zero referenced at the level of the mid-left ventricle under fluoroscopic guidance. Surface ECG was recorded. Hemodynamic data were acquired with the balloon of the pulmonary artery catheter inflated to measure PCWP, while the artificial ventilation was temporarily suspended at end-expiration. Analog signals of ECG, AP, CVP, PVP and PCWP were digitized (200 Hz, 16-bit) by a laboratory computer (ME-B, NEC, Tokyo, Japan), and stored on a hard disk for off-line analysis.

Echocardiographic examinations

Transthoracic echocardiography was performed using an echocardiographic system equipped with a 3.3-MHz transducer (Artida, Toshiba, Tokyo, Japan) [21, 26]. The transducer was directed from the apex to obtain an apical 4-chamber view, and fixed using a mechanical arm. Echocardiogram was recorded simultaneously with acquisition of hemodynamic data, while the artificial ventilation was temporarily suspended at end-expiration. The tricuspid and mitral annular velocities were obtained with pulsed tissue Doppler by placing 2-mm wide sample volumes at the free wall side of the tricuspid annulus [17] and mitral annulus [21], respectively. Transmitral inflow velocity was obtained with pulsed Doppler by placing a 3-mm wide sample volume between the tips of the opened mitral valve leaflets [27]. All Doppler tracings were recorded and stored on the internal hard drive of the echocardiographic system for off-line analysis.

Protocols

Study protocols are schematized in Fig. 1. In all 18 dogs, we first recorded the hemodynamic and echocardiographic data of nonfailing control hearts (NC). We increased preload by infusing 250 mL of 10 % dextran 40 gradually until mean CVP reached 9–11 mmHg. Simultaneous hemodynamic and echocardiographic recordings were repeated 5–7 times per animal, while volume administration was temporarily suspended to maintain steady-state pressures. After data acquisition in NC hearts, we withdrew blood to reduce mean CVP to 3–5 mmHg.

Subsequently, in 6 animals, acute left heart failure (ALHF) was induced by embolizing the left circumflex coronary artery with glass microspheres (90-μm diameter) [14, 21]. We adjusted the number of microspheres to increase mean PCWP by 18 mmHg. In 4 animals, acute right heart failure (ARHF) was induced by embolizing the pulmonary artery with glass microspheres [28], while the balloon of the pulmonary artery catheter was continuously inflated to monitor mean PCWP. We adjusted the number of microspheres to increase mean CVP by 9 mmHg. In ALHF and ARHF animals (Fig. 1), preload was varied by gradually infusing 250 mL of 10 % dextran 40 or withdrawing blood. Simultaneous hemodynamic and echocardiographic recordings were repeated 5–16 times per animal, in the same manner as described above.

In 8 animals, after the first recordings, the venous and arterial catheters were removed, the vessels were repaired, and the incisions were closed using sterile techniques. The animals were allowed to recover for 1 week (Fig. 1). Then, a pacemaker was implanted. Under general anesthesia as described above, a bipolar pacing lead (Model BT-45P,

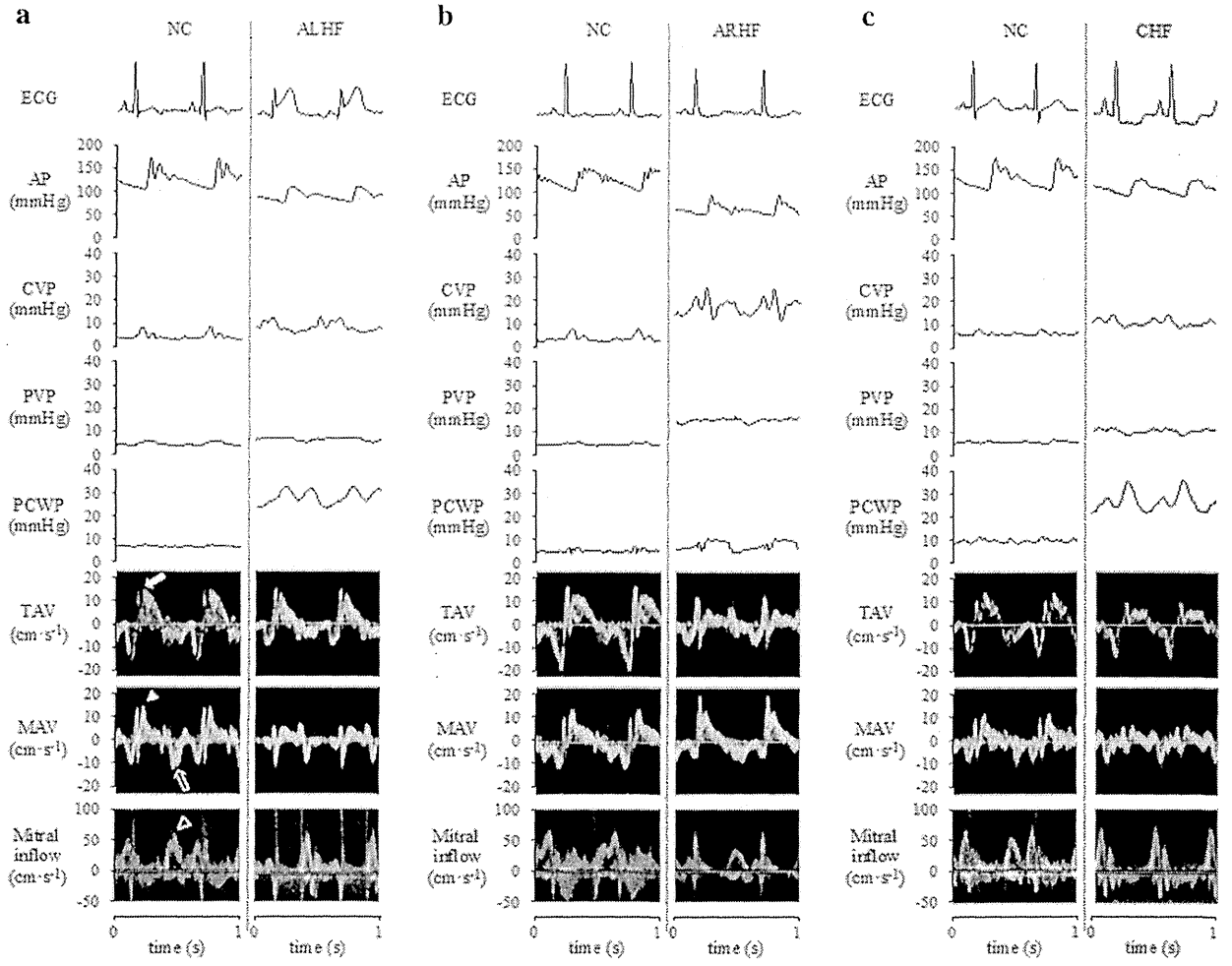

Fig. 2 Representative hemodynamic and echocardiographic tracings in animals allocated to ALHF (**a**), ARHF (**b**), and CHF (**c**) groups. *AP* arterial pressure, *CVP* central venous pressure, *PVP* peripheral venous pressure, *PCWP* pulmonary capillary wedge pressure, *TAV* tricuspid annular velocity, *MAV* mitral annular velocity. *Solid arrow* peak systolic tricuspid annular velocity (S_T), *solid arrow head* peak systolic mitral annular velocity (S_M), *open arrow* peak early diastolic mitral annular velocity (E_a), *open arrow head* peak early diastolic transmitral inflow velocity (E)

Star Medical Inc., Tokyo, Japan) was inserted through the right jugular vein, advanced to the right ventricular apex, and connected to a generator (VOO mode; Model SIP-501, Star Medical Inc., Tokyo, Japan), which was implanted in a subcutaneous pocket in the neck. The incisions were closed, and anesthesia was withdrawn. One day after implantation, rapid ventricular pacing was started at a rate of 220–240 beats/min and continued for 3 weeks to induce chronic biventricular HF (CHF) (Fig. 1) [29]. CHF was confirmed by the presence of HF symptoms including anorexia, lethargy, tachypnea and muscle weakening. After HF was confirmed, pacing was stopped. The CHF animals were anesthetized and prepared for hemodynamic and echocardiographic data recordings as described above. Preload was varied by gradually infusing 250 mL of 10 % dextran 40 or withdrawing blood. Simultaneous hemodynamic and echocardiographic recordings were repeated 5–8 times per animal, in the same manner as described above.

At the conclusion of the experiments, the dogs were euthanized with an intravenous injection of pentobarbital and potassium chloride.

Data analysis

Representative hemodynamic and echocardiographic tracings are shown in Fig. 2. We determined heart rate (HR) from the trace of ECG. AP, CVP, PVP and PCWP data were averaged over 10 s.

Peak velocities during systole of tricuspid annulus (S_T, solid arrow in Fig. 2a) and mitral annulus (S_M, solid arrow

head in Fig. 2a) as well as peak early diastolic velocities of mitral annulus (E_a, open arrow in Fig. 2a) and transmitral inflow (E, open arrow head in Fig. 2a) were measured using a digital Doppler analysis system. Data of echocardiographic variables were expressed as the averages of 3 consecutive cardiac cycles. All echocardiographic analyses were performed off-line by a trained cardiologist (MI) blinded to the hemodynamic data.

Multiple datasets of HR, AP, CVP, PVP, PCWP, S_T, S_M, S_T/S_M, CVP·S_T/S_M PVP·S_T/S_M, E, E_a and E/E_a were determined in each animal. We also calculated absolute changes in PCWP (ΔPCWP), CVP (ΔCVP), CVP·S_T/S_M (ΔCVP·S_T/S_M), PVP·S_T/S_M (ΔPVP·S_T/S_M) and E/E_a ($\Delta E/E_a$) between serial measurements within each animal.

Statistical analysis

All data are presented as mean ± SD. One-way ANOVA with Dunnett's test was used in multiple comparisons for each HF condition relative to NC. Linear regression analysis and the coefficient of determination (R^2) were used to determine the strength of association among the variables. Receiver-operating characteristic (ROC) curve analysis was used to determine optimal cutoff values for selected variables to detect PCWP >18 and >22 mmHg [30]. The area under the ROC curve (AUC) was determined as a summary measure for diagnostic accuracy of the variables. Since accurate estimation of serial changes in PCWP in response to therapy is also important in clinical practice, ROC curve analysis was performed to determine optimal cutoff values for selected variables to predict ΔPCWP >3 and <−3 mmHg. To compare R^2 value of each correlation and AUC of each ROC curve, we used a bootstrap technique (200 replicates) [20, 31]. A P value <0.05 was considered statistically significant. Statistical analyses were performed using commercially available software (Statistica, Statsoft, Inc., Tulsa, OK, USA).

Results

In the 18 dogs, 2 dogs in CHF protocol developed ventricular fibrillation during rapid ventricular pacing, and died before completion of the protocol. From other 16 dogs (6 ALHF, 4 ARHF and 6 CHF dogs), a total of 243 datasets of hemodynamic and echocardiographic variables were obtained (Table 1). We used the datasets to validate the hypothesis that CVP·S_T/S_M reliably predicts PCWP. We compared prediction of PCWP by CVP·S_T/S_M to that by CVP alone.

Of the 16 dogs, PVP data were not available for 3 dogs due to technical errors. From the 13 remaining dogs (5 ALHF, 3 ARHF and 5 CHF dogs), a total of 195 datasets of hemodynamic and echocardiographic variables were obtained (Table 2). We used the datasets to examine whether PVP·S_T/S_M can be used as a minimally invasive alternative to CVP·S_T/S_M in predicting PCWP. We compared prediction of PCWP by PVP·S_T/S_M to that by E/E_a, which is commonly used in clinical practice [3–5].

Range of PCWP achieved in this study (Tables 1, 2) is similar to that seen in advanced HF patients [11].

Prediction of PCWP by CVP·S_T/S_M

In ALHF (Table 1; Fig. 2a), PCWP and CVP were significantly higher, S_T was slightly but significantly lower, S_M was significantly lower, and S_T/S_M was significantly higher than the corresponding values in NC. In ARHF (Table 1; Fig. 2b), CVP but not PCWP was significantly higher, S_T was significantly lower, S_M was significantly higher, and S_T/S_M was significantly lower than the corresponding values in NC. In CHF (Table 1; Fig. 2c), PCWP and CVP were significantly higher, S_T and S_M were significantly lower, and S_T/S_M was significantly higher than the corresponding values in NC. CVP·S_T/S_M was significantly higher in all HF conditions than in NC (Table 1).

A significant but weak correlation was observed between CVP and PCWP (Fig. 3a), while a strong correlation was found between CVP·S_T/S_M and PCWP (Fig. 3b). The R^2 value between CVP·S_T/S_M and PCWP was significantly higher than that between CVP and PCWP ($P < 0.01$). A significant and strong correlation was observed between ΔCVP and ΔPCWP, and also between ΔCVP·S_T/S_M and ΔPCWP (Fig. 3c, d). The R^2 value between ΔCVP·S_T/S_M and ΔPCWP was significantly higher than that between ΔCVP and ΔPCWP ($P < 0.05$).

The ROC curves for CVP and CVP·S_T/S_M in predicting PCWP >18 mmHg are shown in Fig. 3e. The optimal cutoff values were >7.0 mmHg (sensitivity, 72 %; specificity, 57 %) for CVP, and >10.5 mmHg (sensitivity, 85 %; specificity, 88 %) for CVP·S_T/S_M. The ROC curve for CVP·S_T/S_M lay entirely above the curve for CVP. The AUC for CVP·S_T/S_M was significantly larger than that for CVP ($P < 0.01$) (Fig. 3e). ROC analyses of these variables to detect PCWP >22 mmHg (Fig. 3f) yielded similar results. The AUC for CVP·S_T/S_M was significantly larger than that for CVP ($P < 0.01$).

The ROC curves for ΔCVP and ΔCVP·S_T/S_M in predicting ΔPCWP >3 mmHg are shown in Fig. 3g. The optimal cutoff values were >1.0 mmHg (sensitivity, 86 %; specificity, 73 %) for ΔCVP, and >2.0 mmHg (sensitivity, 89 %; specificity, 85 %) for ΔCVP·S_T/S_M. The AUC for ΔCVP and for ΔCVP·S_T/S_M were similar. ROC analyses of these variables to predict ΔPCWP <−3 mmHg (Fig. 3h) produced similar results. The AUC for ΔCVP and for ΔCVP·S_T/S_M were similar.

Table 1 Hemodynamic and echocardiographic data used to evaluate CVP·S_T/S_M

	All datasets ($n = 243$)	Subgroups			
		NC ($n = 94$)	ALHF ($n = 68$)	ARHF ($n = 41$)	CHF ($n = 40$)
HR, bpm	109 ± 13 (71 to 156)	106 ± 14	111 ± 9	102 ± 7	119 ± 17*
AP, mmHg	114 ± 21 (60 to 155)	130 ± 16	98 ± 13*	100 ± 19*	113 ± 7*
CVP, mmHg	7.9 ± 4.0 (−0.5 to 19.4)	5.7 ± 3.3	7.5 ± 2.6*	11.8 ± 2.9*	9.9 ± 4.4*
PCWP, mmHg	17.5 ± 9.2 (1.8 to 40.0)	11.0 ± 5.3	24.4 ± 5.9*	10.3 ± 2.5	28.1 ± 6.6*
S_T, cm/s	11.9 ± 2.9 (5.2 to 21.5)	13.3 ± 2.8	12.1 ± 2.2*	10.6 ± 2.3*	9.7 ± 2.8*
S_M, cm/s	9.4 ± 3.8 (3.4 to 17.6)	11.4 ± 2.8	5.8 ± 1.2*	13.6 ± 2.2*	6.3 ± 1.5*
S_T/S_M	1.5 ± 0.6 (0.5 to 3.4)	1.2 ± 0.3	2.2 ± 0.5*	0.8 ± 0.2*	1.5 ± 0.4*
CVP·S_T/S_M, mmHg	11.1 ± 6.4 (−0.9 to 31.5)	6.7 ± 4.0	16.0 ± 6.2*	9.3 ± 2.9*	14.7 ± 6.2*

Values are presented as mean ± SD (range)

NC normal control, *ALHF* acute left heart failure, *ARHF* acute right heart failure, *CHF* chronic heart failure, *HR* heart rate, *AP* systemic arterial pressure, *CVP* central venous pressure, *PCWP* pulmonary capillary wedge pressure, S_T peak systolic tricuspid annular velocity, S_M peak systolic mitral annular velocity

* $P < 0.01$ against NC

Table 2 Hemodynamic and echocardiographic data used to evaluate PVP·S_T/S_M

	All datasets ($n = 195$)	Subgroups			
		NC ($n = 75$)	ALHF ($n = 59$)	ARHF ($n = 29$)	CHF ($n = 32$)
CVP, mmHg	7.9 ± 3.9 (−0.5 to 19.4)	5.8 ± 3.3	7.7 ± 2.5†	12.2 ± 3.0†	9.5 ± 4.4†
PVP, mmHg	7.7 ± 3.5 (−0.5 to 17.3)	6.4 ± 3.0	6.9 ± 2.3	11.9 ± 2.4†	8.4 ± 4.1†
PCWP, mmHg	18.0 ± 9.4 (1.8 to 40.0)	11.0 ± 5.2	25.0 ± 5.8†	10.7 ± 2.4	28.3 ± 6.7†
CVP·S_T/S_M, mmHg	11.4 ± 6.6 (−0.9 to 31.5)	6.6 ± 3.9	16.7 ± 6.1†	9.5 ± 2.9*	14.4 ± 6.3†
PVP·S_T/S_M, mmHg	10.9 ± 5.7 (−0.6 to 28.7)	7.6 ± 4.0	15.0 ± 5.9†	9.4 ± 2.9	12.6 ± 5.3†
E, cm/s	60 ± 14 (30 to 101)	60 ± 14	59 ± 9	52 ± 10*	70 ± 16†
E_a, cm/s	9.5 ± 2.5 (4.3 to 15.6)	9.8 ± 2.8	8.0 ± 1.3†	11.6 ± 1.5†	9.5 ± 2.2
E/E_a	6.7 ± 1.9 (2.9 to 12.3)	6.4 ± 2.1	7.5 ± 1.1†	4.6 ± 0.9†	7.5 ± 1.4†

Values are presented as mean ± SD (range)

PVP peripheral venous pressure, *E* peak early diastolic transmitral flow velocity, E_a peak early diastolic mitral annular velocity

* $P < 0.05$, † $P < 0.01$ against NC

Minimally invasive prediction of PCWP by PVP·S_T/S_M

PVP·S_T/S_M and PCWP were correlated significantly and tightly (Fig. 4a), while a weak correlation was found between E/E_a and PCWP (Fig. 4b). The R^2 value between PVP·S_T/S_M and PCWP was significantly higher than that between E/E_a and PCWP ($P < 0.01$). A significant and tight correlation was observed between ΔPVP·S_T/S_M and ΔPCWP (Fig. 4c), while a weak correlation was observed between $\Delta E/E_a$ and ΔPCWP (Fig. 4d). The R^2 value between ΔPVP·S_T/S_M and ΔPCWP was significantly higher than that between $\Delta E/E_a$ and ΔPCWP ($P < 0.01$).

The ROC curves for PVP·S_T/S_M and E/E_a in predicting PCWP >18 mmHg are shown in Fig. 4e. The optimal cutoff values were >10.5 mmHg (sensitivity, 73 %; specificity, 84 %) for PVP·S_T/S_M, and >6.0 (sensitivity, 93 %; specificity, 66 %) for E/E_a. The AUC for PVP·S_T/S_M was larger than that for E/E_a with a clear tendency to significance ($P = 0.06$). The ROC curves for these variables in predicting PCWP >22 mmHg are shown in Fig. 4f. The optimal cutoff values were >11.5 mmHg (sensitivity, 72 %; specificity, 79 %) for PVP·S_T/S_M, and >6.5 (sensitivity, 81 %; specificity, 62 %) for E/E_a. The AUC for PVP·S_T/S_M was significantly larger than that for E/E_a ($P < 0.05$).

The ROC curves for ΔPVP·S_T/S_M and $\Delta E/E_a$ in predicting ΔPCWP >3 mmHg are shown in Fig. 4g. The optimal cutoff values were >1.5 mmHg (sensitivity, 90 %; specificity, 78 %) for ΔPVP·S_T/S_M, and >0.0 mmHg (sensitivity, 61 %; specificity, 56 %) for $\Delta E/E_a$. The AUC for ΔPVP·S_T/S_M was significantly larger than that for $\Delta E/E_a$ ($P < 0.01$). ROC analyses of these variables to predict ΔPCWP <−3 mmHg (Fig. 4h) produced similar results. The AUC for ΔPVP·S_T/S_M was significantly larger than that for $\Delta E/E_a$ ($P < 0.01$).

Discussion

The present results validate our hypothesis that CVP·S_T/S_M reliably predicts PCWP, and also suggest that PVP·S_T/S_M may be used as a minimally invasive alternative to CVP·S_T/S_M. To the best of our knowledge, we have for the first time

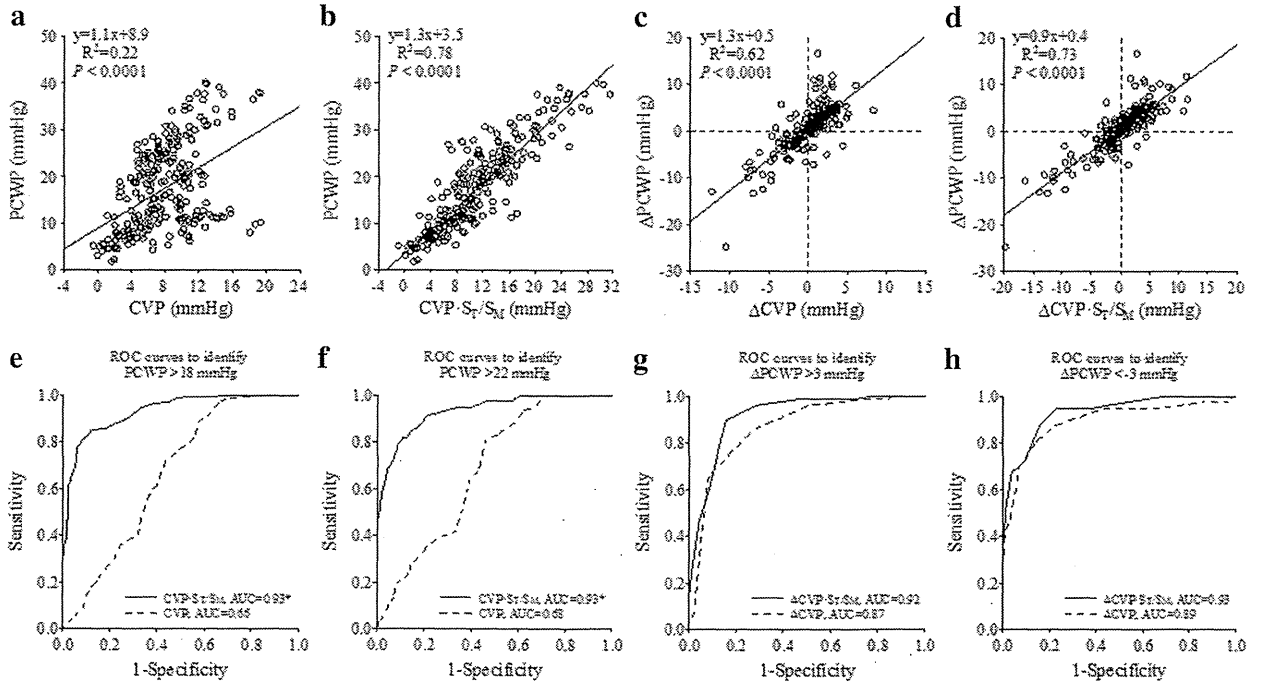

Fig. 3 Relationships between PCWP and CVP (**a**), PCWP and CVP·S_T/S_M (**b**) (243 datasets analyzed). Relationships between serial changes in PCWP (ΔPCWP) and serial changes in CVP (ΔCVP) (**c**), ΔPCWP and serial changes in CVP·S_T/S_M (ΔCVP·S_T/S_M) (**d**) (227 data points analyzed). In panels **a–d**, the regression line, regression equation, coefficient of determination (R^2) and probability value are shown. Receiver-operating characteristic (ROC) curves for the prediction of PCWP >18 mmHg (**e**) and >22 mmHg (**f**) from CVP and CVP·S_T/S_M (243 datasets analyzed). ROC curves for the prediction of ΔPCWP >3 mmHg (**g**) and <−3 mmHg (**h**) from ΔCVP and ΔCVP·S_T/S_M, (227 data points analyzed). AUC indicates area under curve. * $P < 0.01$ versus CVP

successfully integrated the measurement of the venous pressure with echocardiographic assessment of cardiac function to predict PCWP. Indeed, over a wide range of preload, the correlation between CVP·S_T/S_M and PCWP is strong, and better than that between CVP and PCWP. CVP·S_T/S_M predicts abnormal elevation of PCWP more accurately than CVP. The ROC curves for CVP·S_T/S_M to predict abnormal elevation of PCWP and absolute changes in PCWP both had AUC exceeding 0.9, indicating excellent diagnostic accuracy [32]. The correlation between PVP·S_T/S_M and PCWP is tight, and better than that between E/E_a and PCWP. PVP·S_T/S_M predicts abnormal elevation of PCWP reasonably well, and absolute changes in PCWP more accurately than E/E_a. These findings suggest that our technique may be useful not only for the initial single time-point evaluation but also for continuous serial monitoring of PCWP to titrate diuretic or volume loading therapy in the management of HF patients.

S_T/S_M ratio reflects the relationship between RV and LV systolic functions

The S_T/S_M ratio in each HF condition reflected the pathological imbalance between RV and LV functions reasonably well. S_T/S_M was higher in ALHF and lower in ARHF compared to NC (Table 1). Although the pacing-induced CHF model is known to have severe biventricular dysfunction [29], S_T/S_M was significantly higher in CHF animals than that in NC. In this CHF model, LV function may have been more severely depressed relative to RV function. In each HF condition, the pathological imbalance between RV and LV functions was accompanied by a shift of blood between the systemic and pulmonary circuits. When the data in Fig. 3a are classified by cardiac conditions as shown in Fig. 5a, it is clear that for a given CVP, PCWP increases in ALHF and CHF but decreases in ARHF compared to NC. These indicate a shift of blood from the systemic to pulmonary circuits in ALHF and CHF, and in opposite direction in ARHF [10, 13, 14]. As shown in Fig. 5b, correcting CVP by the S_T/S_M ratio (CVP·S_T/S_M) improves the concordance with PCWP irrespective of cardiac conditions. Taken together, although the theoretical model of the relationship between PCWP, CVP, S_T and S_M in Eq. 1 is rather simple, it is both highly predictive and intuitively reasonable.

The assumption that S_T and S_M are related with RVEF [15, 16] and LVEF [18, 19], respectively (Eqs. 7 and 8 in "Materials and methods"), is valid. Our previous study

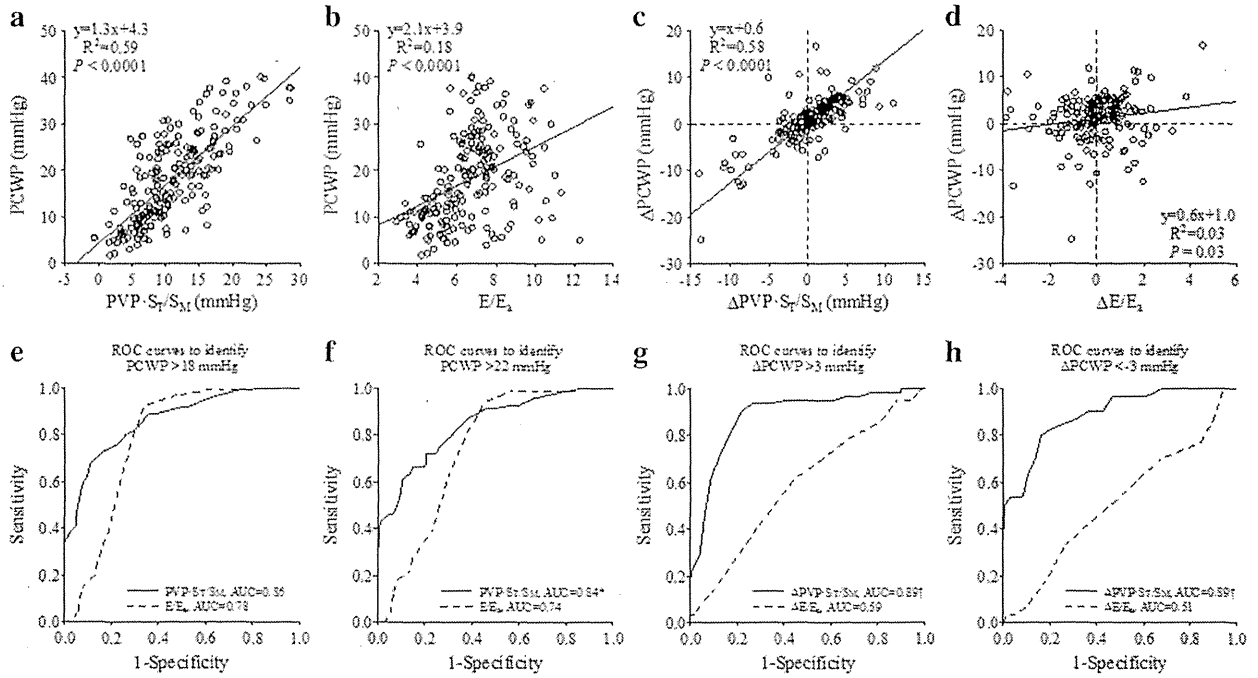

Fig. 4 Relationships between PCWP and PVP·S_T/S_M (**a**), PCWP and E/E_a (**b**) (195 datasets analyzed). Relationships between ΔPCWP and serial changes in PVP·S_T/S_M (ΔPVP·S_T/S_M) (**c**), ΔPCWP and serial changes in E/E_a ($\Delta E/E_a$) (**d**) (182 data points analyzed). In panels **a**–**d**, the regression line, regression equation, coefficient of determination (R^2) and probability value are shown. ROC curves for the prediction of PCWP >18 mmHg (**e**) and >22 mmHg (**f**) from PVP·S_T/S_M and E/E_a (195 datasets analyzed). ROC curves for the prediction of ΔPCWP >3 mmHg (**g**) and <−3 mmHg (**h**) from ΔPVP·S_T/S_M and $\Delta E/E_a$, (182 data points analyzed). * $P < 0.05$ versus E/E_a. † $P < 0.01$ versus $\Delta E/E_a$

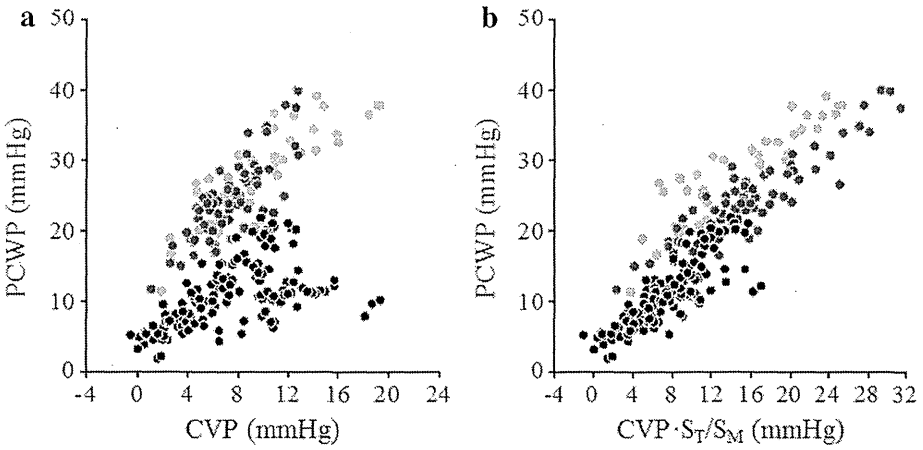

Fig. 5 Relationships of PCWP and CVP (**a**), PCWP and CVP·S_T/S_M (**b**). Each panel shows raw data from all 243 datasets. *Black dot* indicates NC, *red dot* ALHF, *blue dot* ARHF, *green dot* CHF

[21] demonstrated that S_M strongly reflects the status of left ventricular–arterial coupling, which also determines LVEF. S_M itself was not affected by LV preload over a wide range [21].

S_T/S_M ratio can be a clinically useful parameter reflecting the relation between RV and LV systolic function in various types of HF. Some previous results potentially supported this concept. Bruhl et al. [33] demonstrated that S_T/S_M ratio is reproducible and stable across age, body size and gender in a healthy adult population with no cardiac diseases. More interestingly, decreased S_T/S_M ratio predicted pulmonary embolism in patients with HF [34]. Our theoretical analysis (see "Materials and methods") suggests that instead of S_T/S_M ratio, the RVEF to LVEF ratio may be used as a parameter reflecting the relationship between RV and LV functions. However, the EF ratio may

be difficult to obtain by routine clinical echocardiography, because RVEF cannot be measured precisely [15]. Furthermore, assessment of LVEF by routine echocardiography is sometimes difficult especially in obese patients, and patients with pulmonary disease, because precise definition of the endocardial borders is required. Recordings of the tricuspid and mitral annular motion have the practical advantages that they are relatively independent of image quality [18] and are easily done with low (<10 %) inter and intra-operator variability [19].

S_T/S_M ratio can be a noninvasive index of the relation between RV and LV filling pressure. Eq. 1 is rewritten as follows:

$$\mathrm{CVP/PCWP} = 1/(\alpha \cdot S_T/S_M) \quad (11)$$

The relation between S_T/S_M ratio and CVP/PCWP ratio in the 243 datasets (Table 1) indeed tightly approximated a reciprocal function ($\mathrm{CVP/PCWP} = 0.7/(S_T/S_M)$, $R^2 = 0.7$, data not shown), indicating that S_T/S_M ratio and CVP/PCWP ratio are closely related in accordance with our theoretical analysis (see "Materials and methods"). More importantly, S_T/S_M ratio may be used as a noninvasive prognosticator of HF patients. Drazner et al. [35] reported that the ratio of right atrial pressure to PCWP is associated with a risk of adverse outcomes in patients with advanced HF.

Clinical implications

The use of $\mathrm{CVP}\cdot S_T/S_M$ may obviate the need for the pulmonary artery catheterization, which has approximately twice as many catheter-related complications (predominantly arrhythmia) as the central venous catheterization [2]. CVP alone may be useful for serial assessment of changes in PCWP. However, the accuracy of CVP for a single time-point prediction of PCWP is moderate and inferior to that of $\mathrm{CVP}\cdot S_T/S_M$ (Fig. 3e, f). A study in heart transplant candidates showed an increase in proportion of patients with elevated filling pressures demonstrating discordance between RV and LV filling pressures [11], which suggests a potential increase in the necessity of using $\mathrm{CVP}\cdot S_T/S_M$ rather than CVP for reliable prediction of PCWP in the management of patients with advanced HF.

The data of $\mathrm{PVP}\cdot S_T/S_M$ may be acquired even in the outpatient clinic, since PVP can be easily and safely measured by manometry via peripheral venipuncture [22]. In today's clinical practice, PVP is seldom measured. However, the manometric PVP measurements were commonly done until the 1970s in patients suspected of having HF [22]. Although the data of E/E_a are noninvasively obtained, the diagnostic accuracy of E/E_a for the prediction of abnormal elevation of PCWP is moderate and, overall, inferior to that of $\mathrm{PVP}\cdot S_T/S_M$ (Fig. 4e, f). Furthermore, correlation analysis between $\Delta E/E_a$ and ΔPCWP (Fig. 4d), and ROC analysis for $\Delta E/E_a$ to predict ΔPCWP (Fig. 4g, h) indicates that E/E_a has poor diagnostic accuracy in tracking changes in PCWP, which was also reported in previous clinical [6, 7] and experimental [27, 36] studies. In the 195 datasets obtained from the 13 animals (Table 2), the coefficient of determination (R^2) between PCWP and $\mathrm{PVP}\cdot S_T/S_M$ ($R^2 = 0.59$, Fig. 4a) was significantly higher than that between PCWP and CVP ($R^2 = 0.21$) ($P < 0.01$), but was significantly lower than that between PCWP and $\mathrm{CVP}\cdot S_T/S_M$ ($R^2 = 0.78$) ($P < 0.01$) (data not shown). Taken all these together, $\mathrm{PVP}\cdot S_T/S_M$ may not be a perfect, but reasonably reliable alternative to $\mathrm{CVP}\cdot S_T/S_M$.

In clinical practice, physicians estimate CVP noninvasively by visual inspection of jugular pulsation [8], or by echocardiographic examination of cardiovascular dimensions [37, 38]. Clinical evaluation is needed to determine whether echocardiographic measurements of S_T/S_M in conjunction with the noninvasive estimation of CVP can be used to predict PCWP.

Potential sources of error of our technique

The diagnostic accuracy of our technique in the prediction of PCWP may be jeopardized when the assumptions in our theory (see "Materials and methods") are not met. We assume equality of the stroke volumes of RV and LV. In mitral or tricuspid regurgitation, however, the stroke volumes of RV and LV are not equal owing to the presence of various degrees of regurgitant fraction. Some of the HF animals in this study showed mild to moderate degree of tricuspid and/or mitral regurgitation. We also assume a linear relationship between ventricular filling pressure and end-diastolic ventricular volume (Eqs. 5 and 6 in "Materials and methods"). This is not necessary valid especially in LV. The relationship between PCWP and LV end-diastolic ventricular volume can be regarded as linear at low pressures, but approximates curvilinear at high pressures [25, 39].

Restrictive LV filling patterns, a finding known to indicate clinical severity of HF, were also observed in some ALHF and CHF dogs in this study (Fig. 2a, c) [40]. The restrictive LV filling patterns are associated with diastolic ventricular interaction [41]. The direct inter-ventricular interaction is not considered in our theoretical analysis, which might affect the reliability of our technique.

The relation between PCWP and $\mathrm{CVP}\cdot S_T/S_M$, or between PCWP and $\mathrm{PVP}\cdot S_T/S_M$ may vary between subjects. Indeed, linear regression analysis between PCWP and $\mathrm{CVP}\cdot S_T/S_M$ within individual animals indicated that the slope of the regression line varied from 0.6 to 1.7 among the 16 animals (data not shown). Furthermore, the relations

may be modified by the cardiac conditions. PCWP in CHF was higher than that in ALHF, while CVP·S_T/S_M (or PVP·S_T/S_M) in ALHF was higher than that in CHF (Tables 1, 2).

S_T and S_M were recorded only at a single site on the tricuspid annulus and on the mitral annulus, respectively. S_T and S_M thus obtained might not completely reflect global RV and LV function, respectively, because ARHF and ALHF model created in this study possibly had regional myocardial dysfunction [14, 19, 21, 28].

All these might more or less introduce errors in the prediction of PCWP by our technique. However, it is fair to say that even with these potential sources of errors, our technique have enabled us to predict PCWP with acceptable degree of diagnostic accuracy.

Study limitations

The mongrel dogs used in this study were much smaller than human adults, and were anesthetized during data recordings. For validation purpose, we pooled the data of NC animals with the data of animals with very different HF conditions to obtain wide distribution of PCWP, and changed the relation between CVP and PCWP over a wide range. However, this pooled population might be irrelevant in routine clinical practice of HF management.

Clinical relevance of the canine HF models used in this study is limited. The difference between coronary microembolization in healthy dogs to create ALHF and the epicardial coronary occlusion in patients is evident. Tachycardia-induced CHF in dogs and human end-stage HF are different with respect to the time scales of development and persistence of failure. The values of E/E_a noted in HF dogs (Table 2) are smaller than those observed in HF patients [3–7, 42], although they are similar to those reported previously in HF dogs [36]. The E_a values in HF dogs (Table 2) [36] are larger than those in HF patients [3, 42], suggesting that the canine HF models might not have severe diastolic dysfunction observed in HF patients. In relation to this, lack of a diastolic HF model, characterized by HF with preserved EF, may be another limitation of this study. Diastolic HF accounts for approximately 50 % of HF cases [43].

Echocardiography assessment may be affected by inter- and intra-operator variability [44]. In this study, placement of the ultrasound probe on the dog's chest wall and acquisition of Doppler data were conducted by one investigator (KU). Hence, it was impossible to analyze inter- and intra-operator variability of CVP·S_T/S_M or PVP·S_T/S_M.

Further studies are required to address these issues, and to extensively evaluate whether or not our technique can reliably predict PCWP in conscious/anesthetized patients with various types of HF.

Conclusions

CVP corrected by the relationship between RV and LV functions (CVP·S_T/S_M) reliably predicts abnormal elevation and serial changes of PCWP in canine models of various types of HF. PVP·S_T/S_M may be used as a minimally invasive alternative to CVP·S_T/S_M. The present results warrant further research and development of this technique for future clinical application.

Acknowledgments This study was supported by Grant-in-Aid for Scientific Research (C-24500565, C-24591087) from the Ministry of Education, Culture, Sports, Science and Technology, and by Intramural Research Fund (22-1-5, 25-2-1) for Cardiovascular Diseases of National Cerebral and Cardiovascular Center.

Conflict of interest The authors declare no conflict of interest.

References

1. Solomonica A, Burger AJ, Aronson D (2013) Hemodynamic determinants of dyspnea improvement in acute decompensated heart failure. Circ Heart Fail 6:53–60
2. National Heart, Lung, and Blood Institute Acute Respiratory Distress Syndrome (ARDS) Clinical Trials Network, Wheeler AP, Bernard GR, Thompson BT, Schoenfeld D, Wiedemann HP, deBoisblanc B, Connors AF Jr, Hite RD, Harabin AL (2006) Pulmonary-artery versus central venous catheter to guide treatment of acute lung injury. N Engl J Med 354:2213–2224
3. Nagueh SF, Middleton KJ, Kopelen HA, Zoghbi WA, Quiñones MA (1997) Doppler tissue imaging: a noninvasive technique for evaluation of left ventricular relaxation and estimation of filling pressures. J Am Coll Cardiol 30:1527–1533
4. Ommen SR, Nishimura RA, Appleton CP, Miller FA, Oh JK, Redfield MM, Tajik AJ (2000) Clinical utility of Doppler echocardiography and tissue Doppler imaging in the estimation of left ventricular filling pressures: a comparative simultaneous Doppler-catheterization study. Circulation 102:1788–1794
5. Masutani S, Saiki H, Kurishima C, Kuwata S, Tamura M, Senzaki H (2013) Assessment of ventricular relaxation and stiffness using early diastolic mitral annular and inflow velocities in pediatric patients with heart disease. Heart Vessels. doi:10.1007/s00380-013-0422-2
6. Mullens W, Borowski AG, Curtin RJ, Thomas JD, Tang WH (2009) Tissue Doppler imaging in the estimation of intracardiac filling pressure in decompensated patients with advanced systolic heart failure. Circulation 119:62–70
7. Bhella PS, Pacini EL, Prasad A, Hastings JL, Adams-Huet B, Thomas JD, Grayburn PA, Levine BD (2011) Echocardiographic indices do not reliably track changes in left-sided filling pressure in healthy subjects or patients with heart failure with preserved ejection fraction. Circ Cardiovasc Imaging 4:482–489
8. Butman SM, Ewy GA, Standen JR, Kern KB, Hahn E (1993) Bedside cardiovascular examination in patients with severe chronic heart failure: importance of rest or inducible jugular venous distension. J Am Coll Cardiol 22:968–974
9. Drazner MH, Prasad A, Ayers C, Markham DW, Hastings J, Bhella PS, Shibata S, Levine BD (2010) The relationship of right- and left-sided filling pressures in patients with heart failure and a preserved ejection fraction. Circ Heart Fail 3:202–206
10. Forrester JS, Diamond G, McHugh TJ, Swan HJ (1971) Filling pressures in the right and left sides of the heart in acute

myocardial infarction. A reappraisal of central-venous-pressure monitoring. N Engl J Med 285:190–193
11. Campbell P, Drazner MH, Kato M, Lakdawala N, Palardy M, Nohria A, Stevenson LW (2011) Mismatch of right- and left-sided filling pressures in chronic heart failure. J Card Fail 17:561–568
12. Terrovitis JV, Kapelios CJ, Sainis G, Ntalianis A, Kaldara E, Sousonis V, Vakrou S, Michelinakis N, Anagnostou D, Margari Z, Nanas JN (2013) Elevated left ventricular filling pressures can be estimated with accuracy by a new mathematical model. J Heart Lung Transpl 32:511–517
13. Berglund E (1954) Ventricular function. VI. Balance of left and right ventricular output: relation between left and right atrial pressures. Am J Physiol 178:381–386
14. Uemura K, Sugimachi M, Kawada T, Kamiya A, Jin Y, Kashihara K, Sunagawa K (2004) A novel framework of circulatory equilibrium. Am J Physiol Heart Circ Physiol 286:H2376–H2385
15. Wahl A, Praz F, Schwerzmann M, Bonel H, Koestner SC, Hullin R, Schmid JP, Stuber T, Delacrétaz E, Hess OM, Meier B, Seiler C (2011) Assessment of right ventricular systolic function: comparison between cardiac magnetic resonance derived ejection fraction and pulsed-wave tissue Doppler imaging of the tricuspid annulus. Int J Cardiol 151:58–62
16. Meluzín J, Spinarová L, Bakala J, Toman J, Krejcí J, Hude P, Kára T, Soucek M (2001) Pulsed Doppler tissue imaging of the velocity of tricuspid annular systolic motion; a new, rapid, and non-invasive method of evaluating right ventricular systolic function. Eur Heart J 22:340–348
17. Hori Y, Ukai Y, Hoshi F, Higuchi S (2008) Volume loading-related changes in tissue Doppler images derived from the tricuspid valve annulus in dogs. Am J Vet Res 69:33–38
18. Yuda S, Inaba Y, Fujii S, Kokubu N, Yoshioka T, Sakurai S, Nishizato K, Fujii N, Hashimoto A, Uno K, Nakata T, Tsuchihashi K, Miura T, Ura N, Natori H, Shimamoto K (2006) Assessment of left ventricular ejection fraction using long-axis systolic function is independent of image quality: a study of tissue Doppler imaging and m-mode echocardiography. Echocardiography 23:846–852
19. Alam M, Wardell J, Andersson E, Samad BA, Nordlander R (2000) Effects of first myocardial infarction on left ventricular systolic and diastolic function with the use of mitral annular velocity determined by pulsed wave Doppler tissue imaging. J Am Soc Echocardiogr 13:343–352
20. Seo JS, Kim DH, Kim WJ, Song JM, Kang DH, Song JK (2010) Peak systolic velocity of mitral annular longitudinal movement measured by pulsed tissue Doppler imaging as an index of global left ventricular contractility. Am J Physiol Heart Circ Physiol 298:H1608–H1615
21. Uemura K, Kawada T, Sunagawa K, Sugimachi M (2011) Peak systolic mitral annulus velocity reflects the status of ventricular-arterial coupling—theoretical and experimental analyses. J Am Soc Echocardiogr 24:582–591
22. Orient JM (2009) Sapira's art and science of bedside diagnosis. Lippincott Williams & Wilkins, Philadelphia, pp 401–402
23. Amar D, Melendez JA, Zhang H, Dobres C, Leung DH, Padilla RE (2001) Correlation of peripheral venous pressure and central venous pressure in surgical patients. J Cardiothorac Vasc Anesth 15:40–43
24. Sobol I, Barst RJ, Nichols K, Widlitz A, Horn E, Bergmann SR (2004) Correlation between right ventricular ejection fraction obtained with gated equilibrium blood pool spect imaging and right atrial pressure in patients with primary pulmonary hypertension. J Nucl Cardiol 11:S25–S26
25. Greene ES, Gerson JI (1986) One versus two MAC halothane anesthesia does not alter the left ventricular diastolic pressure–volume relationship. Anesthesiology 64:230–237
26. Uemura K, Kawada T, Inagaki M, Sugimachi M (2013) A minimally invasive monitoring system of cardiac output using aortic flow velocity and peripheral arterial pressure profile. Anesth Analg 116:1006–1017
27. Jacques DC, Pinsky MR, Severyn D, Gorcsan J 3rd (2004) Influence of alterations in loading on mitral annular velocity by tissue Doppler echocardiography and its associated ability to predict filling pressures. Chest 126:1910–1918
28. Zwissler B, Forst H, Messmer K (1990) Acute pulmonary microembolism induces different regional changes in preload and contraction pattern in canine right ventricle. Cardiovasc Res 24:285–295
29. Shinbane JS, Wood MA, Jensen DN, Ellenbogen KA, Fitzpatrick AP, Scheinman MM (1997) Tachycardia-induced cardiomyopathy: a review of animal models and clinical studies. J Am Coll Cardiol 29:709–715
30. Zou KH, O'Malley AJ, Mauri L (2007) Receiver-operating characteristic analysis for evaluating diagnostic tests and predictive models. Circulation 115:654–657
31. Skalska H, Freylich V (2006) Web-bootstrap estimate of area under ROC curve. Aust J Stat 35:325–330
32. Swets JA (1988) Measuring the accuracy of diagnostic systems. Science 240:1285–1293
33. Bruhl SR, Chahal M, Khouri SJ (2011) A novel approach to standard techniques in the assessment and quantification of the interventricular systolic relationship. Cardiovasc Ultrasound 9:42
34. Gromadziński L, Targoński R (2007) The role of tissue colour Doppler imaging in diagnosis of segmental pulmonary embolism in congestive heart failure patients. Kardiol Pol 65:1433–1439
35. Drazner MH, Velez-Martinez M, Ayers CR, Reimold SC, Thibodeau JT, Mishkin JD, Mammen PP, Markham DW, Patel CB (2013) Relationship of right- to left-sided ventricular filling pressures in advanced heart failure: insights from the ESCAPE trial. Circ Heart Fail 6:264–270
36. Schober KE, Stern JA, DaCunha DN, Pedraza-Toscano AM, Shemanski D, Hamlin RL (2008) Estimation of left ventricular filling pressure by Doppler echocardiography in dogs with pacing-induced heart failure. J Vet Intern Med 22:578–585
37. Beigel R, Cercek B, Luo H, Siegel RJ (2013) Noninvasive evaluation of right atrial pressure. J Am Soc Echocardiogr 26:1033–1042
38. Hattori H, Minami Y, Mizuno M, Yumino D, Hoshi H, Arashi H, Nuki T, Sashida Y, Higashitani M, Serizawa N, Yamada N, Yamaguchi J, Mori F, Shiga T, Hagiwara N (2013) Differences in hemodynamic responses between intravenous carperitide and nicorandil in patients with acute heart failure syndromes. Heart Vessels 28:345–351
39. Glantz SA, Kernoff RS (1975) Muscle stiffness determined from canine left ventricular pressure–volume curves. Circ Res 37:787–794
40. Solomon SB, Nikolic SD, Glantz SA, Yellin EL (1998) Left ventricular diastolic function of remodeled myocardium in dogs with pacing-induced heart failure. Am J Physiol 274:H945–H954
41. Atherton JJ, Moore TD, Thomson HL, Frenneaux MP (1998) Restrictive left ventricular filling patterns are predictive of diastolic ventricular interaction in chronic heart failure. J Am Coll Cardiol 31:413–418
42. Takaya Y, Taniguchi M, Sugawara M, Nobusada S, Kusano K, Akagi T, Ito H (2013) Evaluation of exercise capacity using wave intensity in chronic heart failure with normal ejection fraction. Heart Vessels 28:179–187
43. Lam CS, Donal E, Kraigher-Krainer E, Vasan RS (2011) Epidemiology and clinical course of heart failure with preserved ejection fraction. Eur J Heart Fail 13:18–28
44. Magda SL, Ciobanu AO, Florescu M, Vinereanu D (2013) Comparative reproducibility of the noninvasive ultrasound methods for the assessment of vascular function. Heart Vessels 28:143–150

Provided for non-commercial research and education use.
Not for reproduction, distribution or commercial use.

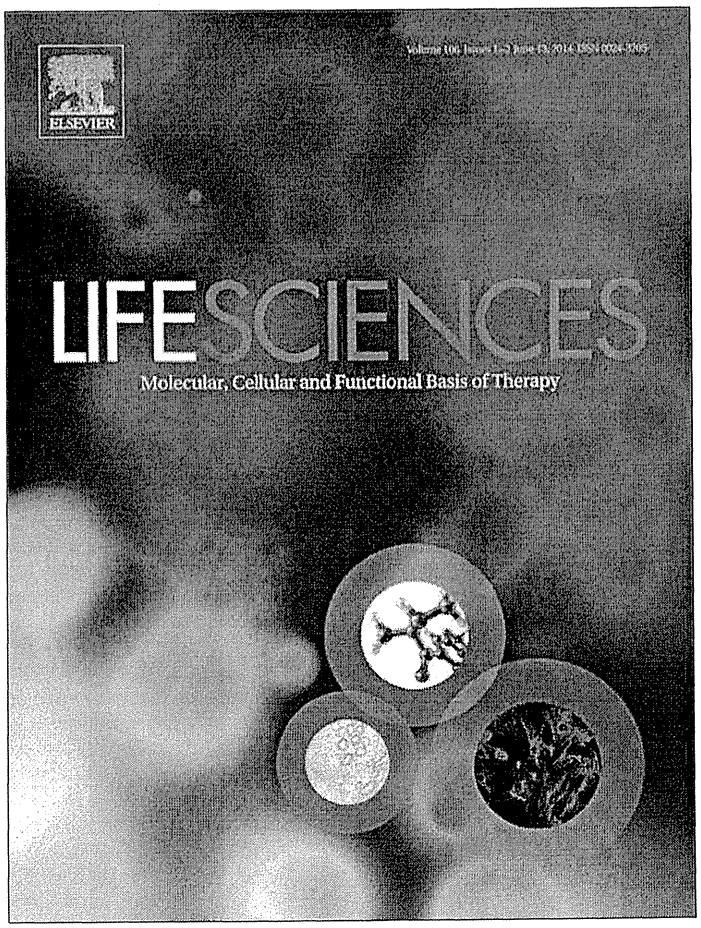

This article appeared in a journal published by Elsevier. The attached copy is furnished to the author for internal non-commercial research and education use, including for instruction at the authors institution and sharing with colleagues.

Other uses, including reproduction and distribution, or selling or licensing copies, or posting to personal, institutional or third party websites are prohibited.

In most cases authors are permitted to post their version of the article (e.g. in Word or Tex form) to their personal website or institutional repository. Authors requiring further information regarding Elsevier's archiving and manuscript policies are encouraged to visit:

http://www.elsevier.com/authorsrights

Author's personal copy

Life Sciences 106 (2014) 40–49

Contents lists available at ScienceDirect

Life Sciences

journal homepage: www.elsevier.com/locate/lifescie

Sustained reduction in blood pressure from electrical activation of the baroreflex is mediated via the central pathway of unmyelinated baroreceptors

Michael J. Turner *, Toru Kawada, Shuji Shimizu, Masaru Sugimachi

Department of Cardiovascular Dynamics, National Cerebral and Cardiovascular Center, Osaka, Japan

ARTICLE INFO

Article history:
Received 13 February 2014
Accepted 17 April 2014
Available online 26 April 2014

Keywords:
Baroreceptor
Baroreflex
Resiniferatoxin
Sympathetic nerve activity

ABSTRACT

Aims: This study aims to identify the contribution of myelinated (A-fiber) and unmyelinated (C-fiber) baroreceptor central pathways to the baroreflex control of sympathetic nerve activity and arterial pressure.
Main methods: Two binary white noise stimulation protocols were used to electrically stimulate the aortic depressor nerve and activate reflex responses from either A-fiber (3 V, 20–100 Hz) or C-fiber (20 V, 0–10 Hz) baroreceptor in anesthetized Sprague-Dawley rats ($n = 10$). Transfer function analysis was performed between stimulation and sympathetic nerve activity (central arc), sympathetic nerve activity and arterial pressure (peripheral arc), and stimulation and arterial pressure (Stim-AP arc).
Key findings: The central arc transfer function from nerve stimulation to splanchnic sympathetic nerve activity displayed derivative characteristics for both stimulation protocols. However, the modeled steady-state gain (0.28 ± 0.04 vs. $4.01 \pm 0.2\% \cdot Hz^{-1}$, $P < 0.001$) and coherence at 0.01 Hz (0.44 ± 0.05 vs. 0.81 ± 0.03, $P < 0.05$) were significantly lower for A-fiber stimulation compared with C-fiber stimulation. The slope of the dynamic gain was higher for A-fiber stimulation (14.82 ± 1.02 vs. 7.21 ± 0.79 dB · decade^{-1}, $P < 0.001$). The steady-state gain of the Stim-AP arc was also significantly lower for A-fiber stimulation compared with C-fiber stimulation (0.23 ± 0.05 vs. 3.05 ± 0.31 mmHg·Hz^{-1}, $P < 0.001$).
Significance: These data indicate that the A-fiber central pathway contributes to high frequency arterial pressure regulation and the C-fiber central pathway provides more sustained changes in sympathetic nerve activity and arterial pressure. A sustained reduction in arterial pressure from electrical stimulation of arterial baroreceptor afferents is likely mediated through the C-fiber central pathway.

© 2014 Elsevier Inc. All rights reserved.

Introduction

The arterial baroreflex is an important negative feedback system that regulates arterial pressure (AP) against acute instabilities during daily activities. Any involvement of the arterial baroreflex in the long-term regulation of AP has been discounted because surgical denervation of baroreceptor afferents fails to chronically increase AP (Guyton, 1980; Cowley, 1992). In hypertension, the arterial baroreflex resets to the prevailing AP and loses the ability to suppress sympathetic nerve activity (SNA) and AP effectively (Krieger, 1986). However, experimental animal studies using electrical stimulation (Lohmeier et al., 2012) and baroreceptor unloading (Thrasher, 2005a) have implied that the arterial baroreflex may be able to chronically control AP. Clinical trials using electrical activation of the carotid sinus baroreflex (Baroreflex activation therapy) have recently demonstrated effective long-term lowering of AP in patients with drug-resistant hypertension (Bakris et al., 2012). Although bypassing the baroreceptor transduction property by directly stimulating the baroreceptor afferent fibers may explain the effectiveness of the baroreflex activation therapy, the neural mechanisms involved in the SNA and AP regulations during electrical stimulation of the baroreceptor afferents are still not well understood.

An often-overlooked issue involved in the clinical application of baroreflex activation therapy is the existence of two types of baroreceptor afferents: myelinated axons (A-fiber) and unmyelinated axons (C-fiber). The former constitutes approximately 10–20% and the latter accounts for the remaining 80–90% of the fibers in the aortic depressor nerve (ADN) of the rat (Fazan et al., 2001). While it has long been known that these axon types differ in a number of functional characteristics such as firing rates, threshold pressures, expression of membrane channels, reflex inhibition of SNA, and transfer function characteristics (Brown et al., 1978; Numao et al., 1985; Thoren et al., 1999; Sun et al., 2009), they may also differ in their central processing of dynamic

* Corresponding author at: Department of Cardiovascular Dynamics, National Cerebral and Cardiovascular Center, 5-7-1 Fujishirodai, Suita, Osaka 565-8565, Japan. Tel.: +81 6 6833 5012x2427; fax: +81 6 6835 5403.
E-mail address: michaeljturner@icloud.com (M.J. Turner).

http://dx.doi.org/10.1016/j.lfs.2014.04.016
0024-3205/© 2014 Elsevier Inc. All rights reserved.

Author's personal copy

input. Previous studies by Kubo et al. (1996) and Petiot et al. (2001) identified the transfer function from ADN stimulation to SNA in rabbits and rats, respectively, but did not deal with differences in fiber type. Furthermore, in studies investigating baroreflex activation therapy, both clinical (Bakris et al., 2012) and animal (Lohmeier et al., 2012), the pulse generator was programmed to target a reduction in AP from hypertensive to control levels. While voltage and frequency guidelines have been used there appears to have been no attempt to actively stimulate either A-fiber or C-fiber baroreceptor afferents and identify their respective contribution to the reduction in AP.

We hypothesized that there is a difference in the dynamic characteristics between A-fiber and C-fiber central pathways, which leads to a difference in the regulation of SNA and AP by each fiber type. Accordingly, the purpose of the present study was to examine the contribution of A- and C-fiber central pathways in the control of SNA and AP by electrically stimulating the left ADN of rats. We devised and utilized dynamic stimulation protocols that preferentially activate A- or C-fiber type baroreceptor afferents.

Materials and methods

Animal preparation

Animal care was provided in strict accordance with the Guiding Principles for the Care and Use of Animals in the Field of Physiological Sciences, approved by the Physiological Society of Japan. All protocols were reviewed and approved by the Animal Subject Committee of the National Cerebral and Cardiovascular Center, Osaka, Japan.

Experiments were completed in 10 male Sprague-Dawley rats (350–450 g). Each rat was anesthetized with an intraperitoneal injection (2 $ml \cdot kg^{-1}$) of a mixture of urethane (250 $mg \cdot ml^{-1}$) and α-chloralose (40 $mg \cdot ml^{-1}$), and mechanically ventilated with oxygen-enriched room air. A venous catheter was inserted into the right femoral vein and 20-fold diluted solution of the above anesthetic mixture was administered to maintain anesthesia (2–3 $ml \cdot kg^{-1} \cdot h^{-1}$). The amount of required anesthesia was determined by testing the withdrawal and blink reflexes and adjusted to maintain AP within a normal range in the absence of ADN stimulation. A heating pad was used to maintain body temperature of the animal at approximately 38 °C. A postganglionic branch of the splanchnic sympathetic nerve was exposed through a left flank incision to record SNA using a pair of stainless steel wire electrodes (Bioflex wire, AS633, Cooner Wire, CA, USA). Silicone glue (Kwik-Sil, World Precision Instruments, FL, USA) was used to secure and insulate the nerve and electrodes (Stocker and Muntzel, 2013). Preamplified nerve signals were band-pass filtered at 150–1000 Hz, and then full-wave rectified and low-pass filtered at a cut-off frequency of 30 Hz using analog circuits to quantify SNA.

Bilateral vagal nerves, carotid sinus nerves and ADNs were sectioned to avoid any confounding effects mediated by native cardiopulmonary and arterial baroreflexes. The sectioned central end of the left ADN was placed on a pair of stainless steel wire stimulating electrodes (Bioflex wire, AS633) and covered with silicone glue (Kwick-Sil). The electrodes were attached to an electrical stimulator (Model SEN-7203, Nihon Kohden, Tokyo, Japan) through a stimulus isolation unit (Model SS-102J, Nihon Kohden).

Stimulation protocols

After surgical procedures were completed, baseline SNA and AP were monitored for 30 min. Two stimulation protocols were employed: step stimulation and dynamic stimulation. The pulse duration of the stimulation was fixed to 0.1 ms. The two stimulation protocols were conducted under control conditions and after a 20-minute perineuronal application of 1 $\mu mol \cdot l^{-1}$ resiniferatoxin (RTX) (LC Laboratories, MA, USA) to the left ADN central to the stimulation site. This dose of RTX can irreversibly block C-fiber conduction without significantly interfering with A-fiber conduction (Reynolds et al., 2006). The sequence of the stimulation protocol was: step – dynamic – dynamic(RTX) – step(RTX).

In the step stimulation protocol ($n = 8$), the left ADN was stimulated for 30 seconds using low-voltage (1–3 V) and high-voltage (18–20 V) settings. These voltages were selected to activate only A-fiber (low voltage) or both A- and C-fibers (high voltage) (Fan and Andresen, 1998; Fan et al., 1999). The high voltage setting is a supramaximal stimulation that is well above the required stimulation intensity to initiate C-fiber baroreceptor action potentials, thus insuring complete recruitment of C-fiber baroreceptors in the ADN. The stimulation frequency was varied among 5, 10, 20, 50 and 100 Hz for each stimulus voltage. The step stimulations were given in random order and 3 minutes apart to allow for full recovery of AP and SNA.

In the dynamic stimulation protocol ($n = 10$), the left ADN was stimulated for 20 minutes. The stimulation frequency was switched between two predefined frequency values every 500 ms according to a computer generated binary white noise sequence. A low-voltage (3 V) and high-frequency (either 20 or 100 Hz) stimulation protocol (LVHf) was used to chiefly estimate dynamic characteristics of the A-fiber baroreceptor central pathway. A high-voltage (20 V) and low-frequency (either 0 or 10 Hz) stimulation protocol (HVLf) was used to chiefly estimate dynamic characteristics of the C-fiber baroreceptor central pathway.

Data analysis

Data were sampled at 200 Hz using a 16-bit analog-to-digital converter. The noise level of SNA was determined by a 10-second average of the SNA signal 2 minutes after intravenous hexamethonium (60 $mg \cdot kg^{-1}$) administration and was defined as zero (Kawada et al., 2010). SNA was normalized by defining the SNA level for 10 seconds preceding the ADN stimulation as 100% activity under control conditions.

In the step stimulation protocol, after applying a 1-second moving average to the data, mean AP (MAP) and SNA responses were quantified as negative changes from the level preceding stimulation (baseline) and designated as ΔMAP and ΔSNA. The negative peak responses and final step responses at 30 seconds were calculated. In the dynamic stimulation protocol, based on 10-Hz resampled data, the transfer function from ADN stimulation to SNA and that from SNA to AP were estimated by using a standard open-loop transfer function analysis described below. The former is referred to as the central arc transfer function and the latter as the peripheral arc transfer function in this paper. The transfer functions from ADN stimulation to AP were also estimated and are referred to as the Stim-AP arc.

Data were analyzed starting from 120 seconds after the initiation of the binary white noise stimulation input. The input–output pairs were resampled at 10 Hz and segmented into 50% overlapping bins of 1024 points each. For each segment, a linear trend was removed, and a Hanning window was applied. Fast Fourier transform was performed to obtain the frequency spectra of the input and output signals. The ensemble averages of the input power spectral density [$S_{XX}(f)$], output power spectral density [$S_{YY}(f)$], and cross spectral density between the input and output signals [$S_{YX}(f)$] were calculated over 12 segments, where f denotes frequency. Finally, the transfer function [$H(f)$] from input to output was estimated as (Bendat and Piersol, 2010):

$$H(f) = \frac{S_{YX}(f)}{S_{XX}(f)} \quad (1)$$

The transfer function is a complex-valued function that can be expressed by the modulus and phase at each frequency. In this study, we refer to the modulus as the dynamic gain. Because the magnitude of SNA varied among animals depending on the recording conditions, two normalization procedures were used. The first normalization procedure, where SNA was normalized by assigning unity to the mean dynamic gain for frequencies below 0.03 Hz, was used for comparison

Author's personal copy

between transfer functions before and after RTX. The second normalization procedure used the noise level of SNA, recorded after the administration of hexamethonium bromide, as zero and the average SNA during baseline recordings was defined as 100%. The second normalization procedure was used for comparisons between A-fiber and C-fiber related transfer functions.

To quantify the linear dependence between the input and output signals, a magnitude squared coherence function [Coh(f)] was calculated as:

$$\mathrm{Coh}(f) = \frac{|S_{YX}(f)|^2}{S_{XX}(f)S_{YY}(f)} \quad (2)$$

The coherence function is a real-valued function ranging from zero to unity. When the output signal is perfectly explained by linear dynamics with the input signal, the coherence value becomes unity. When the output signal is totally independent of the input signal, the coherence value becomes zero.

Simulation

The central and peripheral arc transfer functions were modeled using mathematical transfer functions according to previous studies To facilitate understanding of SNA and AP regulation via the A-fiber and C-fiber pathways, the central and peripheral transfer functions were modeled. According to previous studies (Kawada et al., 2002, 2010) the central arc transfer functions were modeled as:

$$H_N(f) = K_N \frac{1+\frac{f}{f_{C1}}j}{\left(1+\frac{f}{f_{C2}}j\right)^2} \exp(-2\pi\ f\ L_N j) \quad (3)$$

where j represents the imaginary units. K_N is the steady-state gain of the central arc (in %·Hz^{-1}), f_{C1} is the corner frequency determining the derivative characteristics (in Hz), f_{C2} is the corner frequency determining the high-cut characteristics (in Hz), and L_N is the pure dead time (in seconds).

The peripheral arc transfer functions were modeled by a second-order low-pass filter as:

$$H_P(f) = \frac{K_P}{1+2\zeta\frac{f}{f_N}j+\left(\frac{f}{f_N}j\right)^2} \exp(-2\pi f L_P j) \quad (4)$$

where K_P is the steady-state gain of the peripheral arc (in mmHg·%$^{-1}$), f_N is the natural frequency (in Hz), ζ is the damping ratio (unitless), and L_P is the pure dead time (in seconds). To facilitate understanding of the modeled transfer function, step responses were calculated by deriving the system impulse response from the inverse Fourier transform. The step response was then obtained from the time integral of the impulse response (Kawada et al., 2002, 2010). The Stim-AP arc was calculated from a product of the central and peripheral arc transfer functions in the frequency domain. To further aid in understanding of the transfer functions, step responses in the time domain, corresponding to respective model transfer functions were also calculated.

Statistical analysis

All data are presented as mean and standard error. Effects of stimulation frequency and RTX on ΔMAP and ΔSNA in the step stimulation protocol were examined by repeated measures two-way ANOVA. The effect of RTX at each frequency was then examined by paired t-test with Bonferroni correction. Before and after the RTX application, changes in mean SNA and AP levels were examined using repeated measures ANOVA followed by paired t-test with Bonferroni correction for comparisons among conditions of pre-stimulation, LVHf, and HVLf stimulation. The transfer function values (dynamic gain and phase) at 0.01, 0.1 and 1 Hz were also compared using repeated measures ANOVA followed by paired t-test with Bonferroni correction among conditions of LVHf before RTX, LVHf after RTX, HVLf before RTX, and HVLf after RTX. Coherence values were compared using Friedman's test with post-hoc Dunn's multiple comparison test. Differences were considered to be significant at $P < 0.05$ for all statistical analysis.

Results

Low-voltage step stimulation

Representative traces of low-voltage step stimulation at 50 Hz before and after perineuronal application of RTX are shown in Fig. 1a. While stimulation decreased MAP and SNA, the reflex decreases in MAP and SNA returned towards pre-stimulation levels during the 30-second stimulation period. RTX had no significant effect on the SNA and MAP responses. The negative peak responses and the final responses measured at different stimulation frequencies are summarized in Fig. 1b. Low intensity stimulation of the ADN lowered SNA and MAP between 20 and 100 Hz, which was unaffected by the application of RTX.

High-voltage step stimulation

Representative traces of high-voltage step stimulation at 20 Hz before and after perineuronal application of RTX are shown in Fig. 2a. The reflex response in MAP was well sustained during the 30-second stimulation period under the control condition. After the RTX application, the negative peak response and the final response became smaller, and the reduction of MAP was not sustained and returned towards baseline levels. The negative peak responses and the final responses measured at different stimulation frequencies are summarized in Fig. 2b. Large reflex responses in SNA and MAP were observed at 5 Hz and above before RTX application.

Dynamic stimulation

Typical experimental traces during the LVHf and HVLf dynamic stimulation protocols before and after perineuronal application of RTX are shown in Fig. 3. MAP and SNA were not significantly decreased from baseline values by the LVHf stimulation, both before and after the RTX application (Table 1). However, MAP and SNA were significantly decreased from baseline values by the HVLf stimulation before RTX application (MAP: 101 ± 2.7 mmHg compared with 79.4 ± 2.4 mmHg, $P < 0.01$; SNA: 100% compared with 70.4 ± 2.5%, $P < 0.001$). RTX abolished the reduction in MAP and SNA observed during the HVLf stimulation (MAP: 105 ± 3.3 mmHg compared with 99.9 ± 4.4 mmHg, SNA: 116 ± 11% compared with 112.4 ± 8.7%).

Central and peripheral arc transfer functions

The central arc transfer function from ADN stimulation to SNA determined by either LVHf or HVLf stimulation shows that normalized dynamic gain increases as the modulation frequency increases (Fig. 4a). The slope of the dynamic gain and dynamic gain at 1 Hz were significantly smaller for the central arc transfer function estimated by HVLf stimulation (7.21 ± 0.79 dB·decade^{-1}, Fig. 4a, right) than those estimated by LVHf stimulation (14.82 ± 1.02 dB · decade^{-1}, $P < 0.001$, Fig. 4a, left). The coherence of the transfer function estimated by HVLf was significantly higher compared with LVHf stimulation at 0.01 Hz (0.81 ± 0.03 and 0.44 ± 0.05, $P < 0.05$) and 0.1 Hz (0.77 ± 0.04 and 0.42 ± 0.08, $P < 0.05$). The phase of both transfer functions was close to $-\pi$ radians in the lower frequencies, reflecting the out-of-phase relationship between ADN stimulation and SNA. RTX had little effect on the central arc transfer function estimated by the LVHf stimulation other than an increased dynamic gain at 0.1 Hz (Table 2). However, RTX significantly decreased the dynamic gain of HVLf simulation at modulation frequencies of 0.01 Hz (1.10 ± 0.02 a.u.·Hz^{-1} compared with 0.39 ±

Author's personal copy

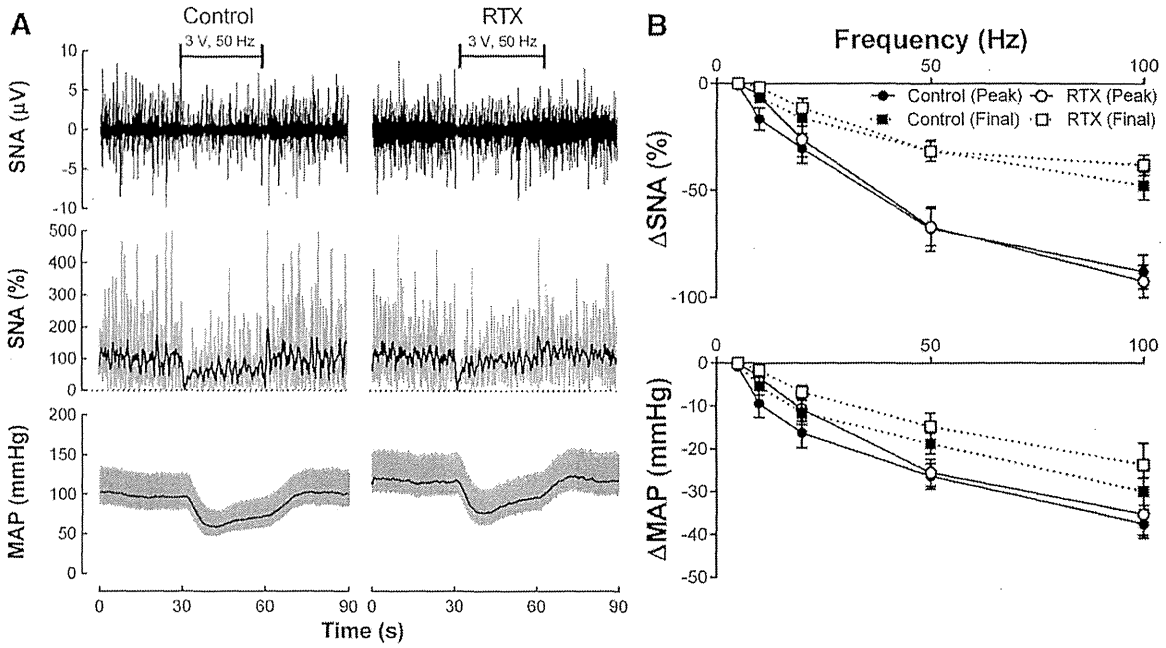

Fig. 1. Sympathetic nerve activity (SNA) and mean arterial pressure (MAP) responses to low voltage (3 V) stimulation. (a) Representative traces showing reflex responses in SNA (top) and MAP (bottom) from electrical stimulation of the ADN at 3 V, 50 Hz. After a transient baroreflex response, SNA and MAP returned towards pre-stimulation levels during the 30-second stimulation period. The gray lines indicate the original 200 Hz signal and the black lines are a 1-second moving average signal. (b) Group data ($n = 8$ in each group) shows high-frequency stimulation of 20 Hz and above was required to evoke notable reflex decreases in SNA (top) and MAP (bottom). At the stimulation frequencies of 20 Hz and above, the magnitude of the final responses (■) in SNA and MAP was approximately 50% and 70–80% of the peak responses (●), respectively. RTX did not significantly affect the negative peak responses (○) or the final responses (□).

0.04 a.u.·Hz^{-1}, $P < 0.01$) and 0.1 Hz (1.27 ± 0.12 a.u.·Hz^{-1} and 0.38 ± 0.04 a.u.·Hz^{-1}, $P < 0.01$) and coherence values at 0.01 Hz (0.81 ± 0.03 and 0.24 ± 0.05, $P < 0.001$), 0.1 Hz (0.77 ± 0.04 and 0.29 ± 0.06, $P < 0.001$) and 1 Hz (0.70 ± 0.04 and 0.33 ± 0.06, $P < 0.05$).

The peripheral transfer function from SNA to AP estimated by either LVHf or HVLf stimulation shows that normalized dynamic gain decreases as the modulation frequency increases (Fig. 4b). The phase of both transfer functions approached zero radians at 0.01 Hz and was delayed by almost -2π radians as the modulation frequency increased to 1 Hz. RTX had no effect on the peripheral arc transfer function estimated by LVHf stimulation (Table 3). RTX significantly decreased the dynamic gain at 0.01 Hz (0.99 ± 0.06 mmHg·a.u.$^{-1}$ and 0.57 ±

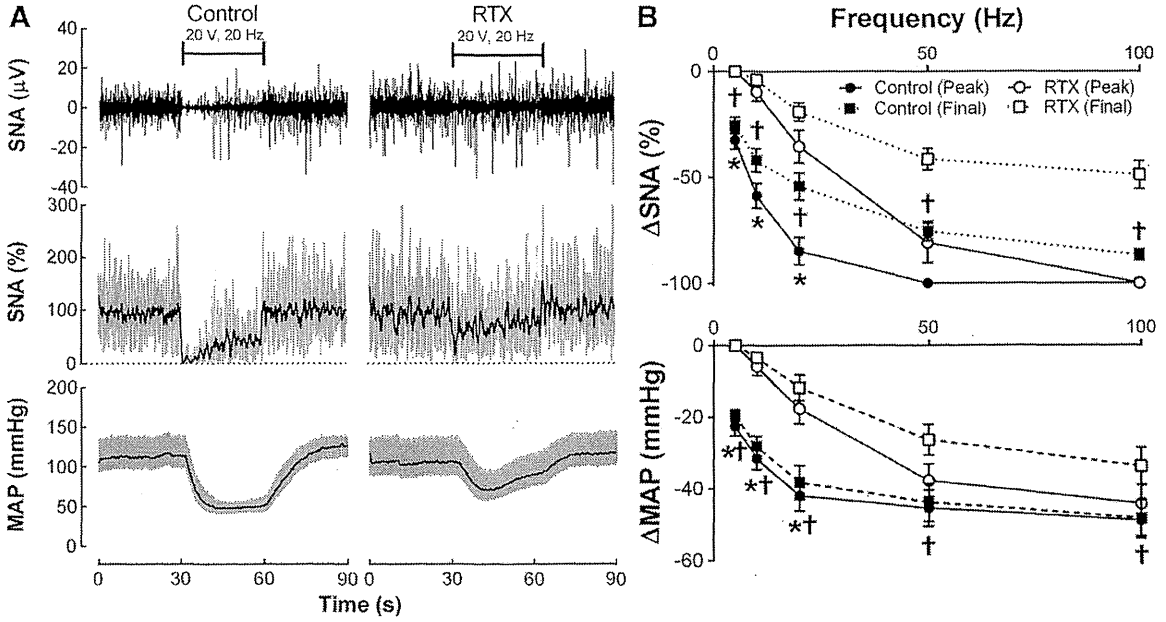

Fig. 2. Sympathetic nerve activity (SNA) and mean arterial pressure (MAP) responses to high voltage (20 V) stimulation. (a) Representative traces showing reflex responses in SNA (top) and MAP (bottom) from electrical stimulation of the ADN at 20 V, 20 Hz. High voltage stimulation resulted in robust responses in SNA and MAP that was sustained throughout the stimulation period. After the application of RTX, responses became brief and returned towards pre-stimulation levels while stimulation was maintained. The gray lines indicate the original 200 Hz signal and the black lines are a 1-second moving average signal. (b) Group data ($n = 8$ in each group) shows that the magnitude of the final responses (■) in SNA and MAP was above 60% and 90% of the peak responses (●), respectively. RTX significantly attenuated the negative peak responses (○) at 5 Hz, 10 Hz, and 20 Hz and the final responses (□) at all frequencies for both SNA and MAP. *$P < 0.01$ for control (peak) vs. RTX (peak); †$P < 0.01$ for control (final) vs. RTX (final).

Author's personal copy

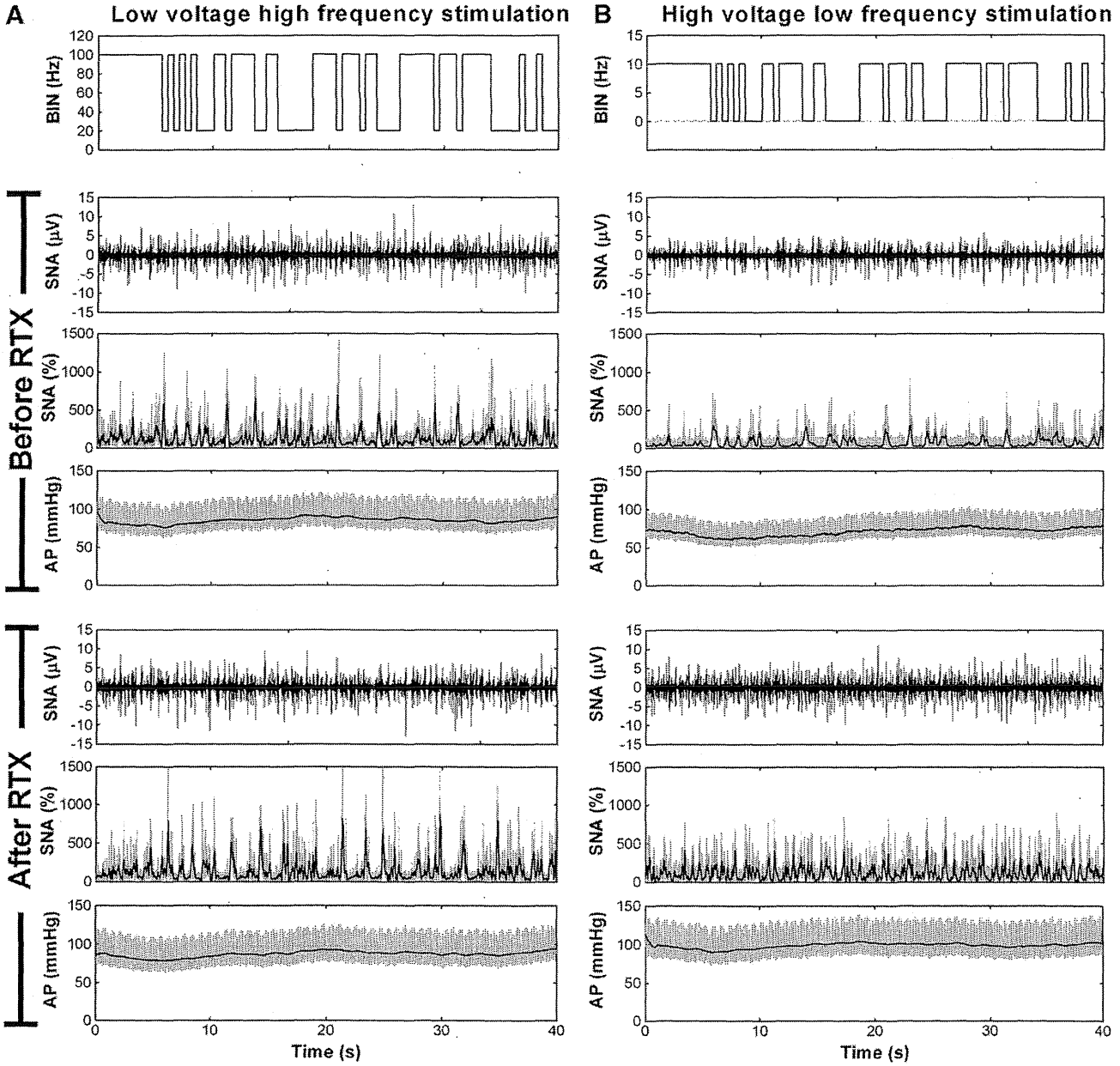

Fig. 3. Typical recordings of binary white noise stimulation (BIN), sympathetic nerve activity (SNA) and arterial pressure (AP) during low voltage (3 V) high frequency stimulation (a) and high voltage (20 V) low frequency stimulation (b). Because of the dynamic nature of the input signal it is not easy to visually identify stimulation-induced reflex responses in SNA and AP. In the SNA plots, the gray lines are the 200 Hz signal, and the black lines indicate 10 Hz resampled data and in the AP plots, the gray lines are the 200 Hz signal and the black line indicates a 1-second moving average.

Table 1
Cardiovascular variables during pre-stimulation conditions and stimulation protocols.

	Before RTX			After RTX		
	Prestim	LVHf	HVLf	Prestim	LVHf	HVLf
SNA, %	100	96.3 ± 11.0	70.4 ± 2.5[a,b]	116 ± 11.0	106 ± 6.9	112 ± 8.7
MAP, mmHg	101 ± 2.7	96.0 ± 5.6	79.4 ± 2.4[c,d]	105 ± 3.3	94.3 ± 4.7	99.9 ± 4.4
HR, bpm	387 ± 6.2	394 ± 10.1	370 ± 9.0	394 ± 6.3	408 ± 10.8	404 ± 4.7

Data are means ± SE (n = 10 in each group). SNA, sympathetic nerve activity; MAP, mean arterial pressure; HR, heart rate; Prestim, pre-stimulation conditions; LVHf, low-voltage high-frequency dynamic stimulation; HVLf, high-voltage low-frequency dynamic stimulation; RTX, resiniferatoxin.

[a] $P < 0.001$ vs. Prestim.
[b] $P < 0.001$ vs. LVHf.
[c] $P < 0.01$ vs. Prestim.
[d] $P < 0.05$ vs. LVHf.

Author's personal copy

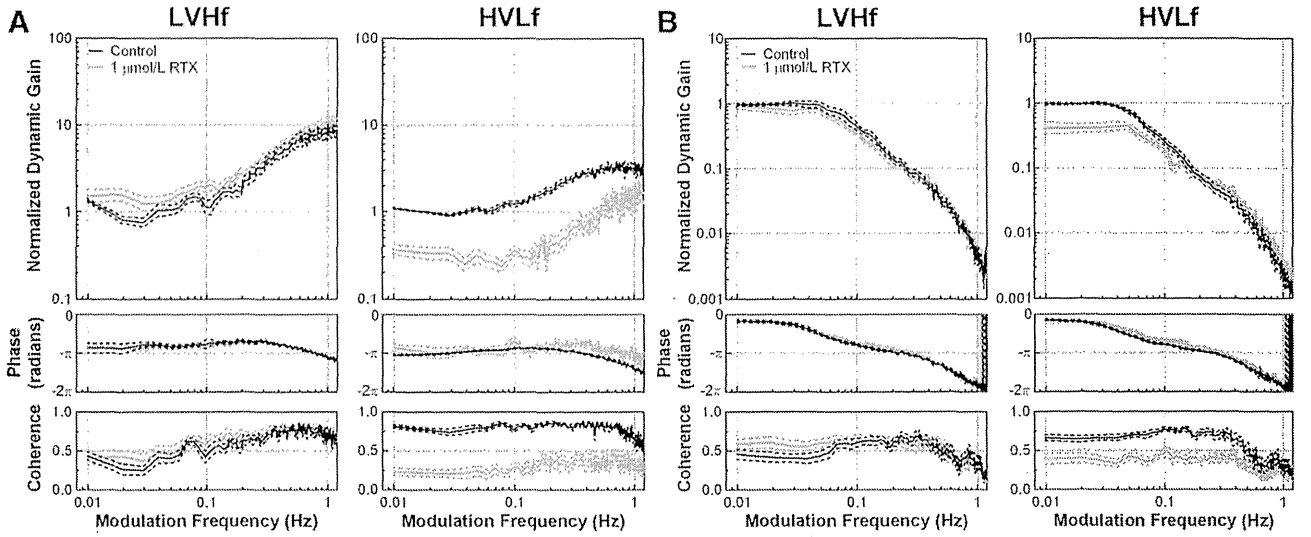

Fig. 4. Effect of RTX on central arc (a) and peripheral arc (b) transfer functions using either LVHf (left) or HVLf (right) stimulation protocols. LVHf, low-voltage high-frequency dynamic stimulation; HVLf, high-voltage low-frequency dynamic stimulation; RTX, resiniferatoxin. In each panel, the solid and dashed lines represent the mean and mean ± SE, respectively.

0.07 mmHg·a.u.$^{-1}$, $P < 0.001$) and coherence values at 0.01 Hz (0.66 ± 0.04 and 0.39 ± 0.07, $P < 0.05$) and 0.1 Hz (0.77 ± 0.02 and 0.46 ± 0.06, $P < 0.001$) of the peripheral arc transfer function estimated by HVLf stimulation.

Stim-AP arc transfer functions

The Stim-AP arc transfer function, estimated by either LVHf or HVLf stimulation, shows that normalized dynamic gain decreases as the modulation frequency increases (Fig. 5). The phase of both transfer functions approached $-\pi$ radians at 0.01 Hz and was delayed by almost -3π radians as the modulation frequency increased to 1 Hz. RTX had no effect on the Stim-AP arc transfer function estimated by LVHf stimulation (Table 4). RTX significantly decreased the dynamic gain at 0.01 Hz (3.05 ± 0.31 mmHg·Hz^{-1} and 0.91 ± 0.10 mmHg·Hz^{-1}, $P < 0.001$)

Table 2
Transfer function parameters of the baroreflex central arc obtained from LVHf and HVLf stimulation protocols.

Central arc	LVHf	LVHf (RTX)	HVLf	HVLf (RTX)
Gain (a.u.·Hz^{-1})				
0.01 Hz	1.39 ± 0.07	1.69 ± 0.23	1.10 ± 0.02	0.39 ± 0.04[a]
0.1 Hz	1.28 ± 0.2	2.07 ± 0.28[c]	1.27 ± 0.12	0.38 ± 0.04[a]
1 Hz	8.55 ± 1.06	10.28 ± 1.13	3.36 ± 0.23[b]	1.72 ± 0.26
Slope (dB·decade^{-1})				
0.1–1 Hz	14.82 ± 1.02	15.54 ± 1.32	7.21 ± 0.79[b]	15.94 ± 1.64[d]
Phase (radians)				
0.01 Hz	−2.68 ± 0.23	−2.52 ± 0.11	−3.27 ± 0.05	−2.72 ± 0.3
0.1 Hz	−2.74 ± 0.36	−2.51 ± 0.16	−2.72 ± 0.05	−2.54 ± 0.46
1 Hz	−3.36 ± 0.09	−3.31 ± 0.09	−4.24 ± 0.09[b]	−3.18 ± 0.15[d]
Coherence				
0.01 Hz	0.44 ± 0.05	0.40 ± 0.08	0.81 ± 0.03[e]	0.24 ± 0.05[d]
0.1 Hz	0.42 ± 0.08	0.57 ± 0.07	0.77 ± 0.04[e]	0.29 ± 0.06[d]
1 Hz	0.70 ± 0.05	0.73 ± 0.04	0.70 ± 0.04	0.33 ± 0.06[f]

Data are means ± SE ($n = 10$ in each group). LVHf, low-voltage high-frequency dynamic stimulation; HVLf, high-voltage low-frequency dynamic stimulation; RTX, resiniferatoxin.
[a] $P < 0.01$ vs. HVLf.
[b] $P < 0.001$ vs. LVHf.
[c] $P < 0.01$ vs. LVHf.
[d] $P < 0.001$ vs. HVLf.
[e] $P < 0.05$ vs. LVHf.
[f] $P < 0.05$ vs HVLf.

and coherence values at 0.01 Hz (0.70 ± 0.03 and 0.31 ± 0.07, $P < 0.001$) and 0.1 Hz (0.72 ± 0.04 and 0.41 ± 0.07, $P < 0.01$) of the Stim-AP arc transfer function estimated by HVLf stimulation. The gain at 0.01 Hz was also significantly lower for the transfer function estimated by LVHf stimulation compared with HVLf (0.23 ± 0.05 mmHg·Hz^{-1} and 3.05 ± 0.31 mmHg·Hz^{-1}, $P < 0.001$).

Simulation

Model transfer functions and corresponding step responses are shown in Fig. 6. The parameter values used to simulate the transfer functions were derived from the mean values shown in Table 5. The transfer gain in the lower frequency range (steady-state) was lower in the A-fiber related transfer function than the C-fiber related transfer function in the central arc (0.28 ± 0.04%·Hz^{-1} vs. 4.01 ± 0.2%·Hz^{-1}, $P < 0.001$) and Stim-AP arc (0.15 ± 0.03 mmHg·Hz^{-1} vs. 2.39 ± 0.23 mmHg·Hz^{-1}, $P < 0.001$). There were no significant differences between the A-fiber and C-fiber related transfer functions of the peripheral arc (Table 4). The step responses, corresponding to the respective model transfer functions, provide an intuitive representation of A- and C-fiber related changes in SNA and AP. The peak response was significantly greater (−11.20 ± 0.50% vs. −2.44 ± 0.44%, $P < 0.001$) and time to peak (0.36 ± 0.02 second vs. 0.19 ± 0.01 second, $P < 0.001$) was significantly longer for C-fiber related responses in the central arc step response. There was no significant difference in the peripheral arc step responses.

Discussion

The purpose of this study was to identify the contribution of A- and C-fiber baroreceptor central pathways to the reduction in AP observed during electrical activation of the arterial baroreflex. The present results demonstrate that the C-fiber central pathway contributes more to sustained decreases in SNA and AP than the A-fiber central pathway.

Dynamic characteristics of A- and C-fiber central pathways

Arterial baroreceptors can be classified as either A- or C-fiber type based on the presence of myelin and other distinct characteristics, such as firing rate and threshold pressures. While the differences in firing characteristics of A- and C-fiber baroreceptor afferents are well documented (Thoren et al., 1999), differences in the central processing

Author's personal copy

Table 3
Transfer function parameters of the baroreflex peripheral arc obtained from LVHf and HVLf stimulation protocols.

Peripheral arc	LVHf	LVHf(RTX)	HVLf	HVLf(RTX)
Gain (mmHg·a.u.$^{-1}$)				
0.01 Hz	0.97 ± 0.06	0.98 ± 0.01	0.99 ± 0.06	0.57 ± 0.07[a]
0.1 Hz	0.52 ± 0.08	0.38 ± 0.03	0.29 ± 0.03[b]	0.21 ± 0.02
1 Hz	0.007 ± 0.001	0.007 ± 0.001	0.003 ± 0.001[c]	0.005 ± 0.001
Slope (dB·decade^{-1})				
0.1–1 Hz	−32.6 ± 0.94	−29.3 ± 2.17	−34.3 ± 1.05	−26 ± 1.72[a]
Phase (radians)				
0.01 Hz	−0.56 ± 0.11	−0.53 ± 0.06	−0.44 ± 0.07	−0.66 ± 0.17
0.1 Hz	−2.41 ± 0.12	−2.33 ± 0.12	−2.44 ± 0.08	−2.11 ± 0.14[d]
1 Hz	−4.98 ± 0.29	−5.01 ± 0.29	−5.18 ± 0.19	−5.27 ± 0.13
Coherence				
0.01 Hz	0.45 ± 0.06	0.59 ± 0.06	0.66 ± 0.04	0.39 ± 0.07[d]
0.1 Hz	0.60 ± 0.06	0.67 ± 0.04	0.77 ± 0.02[c]	0.46 ± 0.06[a]
1 Hz	0.36 ± 0.07	0.33 ± 0.06	0.32 ± 0.06	0.30 ± 0.05

Data are means ± SE (n = 10 in each group). LVHf, low-voltage high-frequency dynamic stimulation; HVLf, high-voltage low-frequency dynamic stimulation; RTX, resiniferatoxin.
[a] $P < 0.001$ vs. HVLf.
[b] $P < 0.01$ vs. LVHf.
[c] $P < 0.05$ vs LVHf.
[d] $P < 0.05$ vs. HVLf.

between A-fiber and C-fiber central pathways remain to be fully elucidated. The present study demonstrated that LVHf dynamic stimulation, which predominantly activates the A-fiber baroreceptor afferents, produced a central arc transfer function with strong derivative characteristics (Fig. 4a, left). This may indicate that the A-fiber central pathway primarily contributes to the SNA regulation in the higher frequency range. In contrast, HVLf dynamic stimulation, which predominantly activates the C-fiber baroreceptor afferents, produced a central arc transfer function with less derivative characteristics before the RTX application (Fig. 4a, right). Therefore, the C-fiber central pathway contributes to the SNA regulation both in the lower frequency range and in the higher frequency range. These characteristics conform to known characteristics of A- and C-fiber baroreceptor firing (Thoren et al., 1999).

The dynamic gain of the C-fiber related central arc transfer function was over an order of magnitude higher than that of the A-fiber related central arc transfer function (Fig. 6a). These data indicate that, per unit stimulation frequency, C-fiber baroreceptor activity results in a significantly greater reduction in SNA than A-fiber baroreceptor activity. At the same time, it is important to remember normal physiological firing rates of A-fiber (10–100 Hz) and C-fiber (0–20 Hz) baroreceptor axons (Thoren et al., 1999). Even after we take this difference into account it seems that the C-fiber central pathway contributes more to the SNA regulation in the lower frequency range compared with the A-fiber central pathway. The simulation of the Stim-AP arc (Fig. 6c) also indicates that the contribution of the C-fiber pathway is greater in the regulation of AP than that of A-fiber pathway because the peripheral arc transfer function did not differ significantly between A- and C-fiber related transfer functions (Fig. 6b).

To further interpret how each baroreceptor subtype contributes to the control of SNA it is important to take coherence into account.

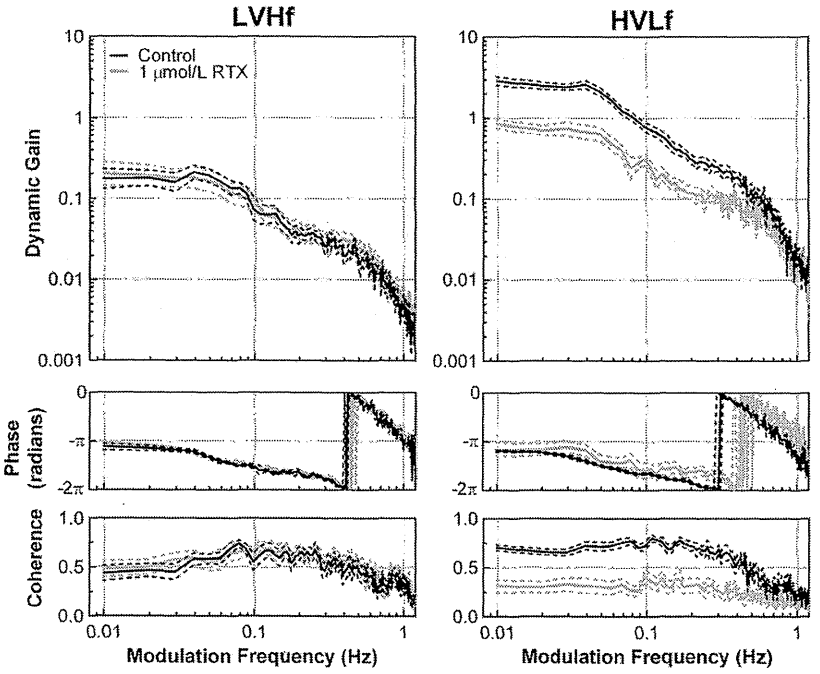

Fig. 5. Effect of RTX on Stim-AP arc transfer functions using either LVHf (left) or HVLf (right) stimulation protocols. LVHf, low-voltage high-frequency dynamic stimulation; HVLf, high-voltage low-frequency dynamic stimulation; RTX, resiniferatoxin. In each panel, the solid and dashed lines represent the mean and mean ± SE, respectively.

Author's personal copy

Table 4
Transfer function parameters of the Stim-AP arc obtained from LVHf and HVLf stimulation protocols.

Stim-AP Arc	LVHf	LVHf (RTX)	HVLf	HVLf (RTX)
Gain (mmHg·Hz^{-1})				
0.01 Hz	0.23 ± 0.05	0.29 ± 0.06	3.05 ± 0.31[b]	0.91 ± 0.10[a]
0.1 Hz	0.10 ± 0.02	0.10 ± 0.02	0.83 ± 0.10[b]	0.35 ± 0.06[a]
1 Hz	0.006 ± 0.001	0.008 ± 0.002	0.026 ± 0.004[b]	0.024 ± 0.003
Slope (dB·decade^{-1})				
0.1–1 Hz	−18.6 ± 1.40	−16.5 ± 1.34	−23.4 ± 0.87[c]	−15.6 ± 1.07[a]
Phase (radians)				
0.01 Hz	−3.50 ± 0.22	−3.25 ± 0.11	−3.73 ± 0.06	−3.12 ± 0.46
0.1 Hz	−4.73 ± 0.16	−4.78 ± 0.13	−5.19 ± 0.07	−4.43 ± 0.46
1 Hz	−5.95 ± 0.15	−5.61 ± 0.10	−6.80 ± 0.13[d]	−5.90 ± 0.21[c]
Coherence				
0.01 Hz	0.44 ± 0.08	0.48 ± 0.08	0.70 ± 0.03	0.31 ± 0.06[a]
0.1 Hz	0.55 ± 0.08	0.65 ± 0.05	0.72 ± 0.04	0.41 ± 0.07[a]
1 Hz	0.32 ± 0.05	0.38 ± 0.05	0.25 ± 0.04	0.19 ± 0.03

Data are means ± SE (n = 10 in each group). LVHf, low-voltage high-frequency dynamic stimulation; HVLf, high-voltage low-frequency dynamic stimulation; RTX, resiniferatoxin.
[a] $P < 0.001$ vs. HVLf.
[b] $P < 0.001$ vs. LVHf.
[c] $P < 0.01$ vs. HVLf.
[d] $P < 0.01$ vs. LVHf.
[e] $P < 0.05$ vs. LVHf.

Table 5
Model parameters and step response.

	A-fiber related	C-fiber related
Central arc		
K_N, %·Hz^{-1}	0.278 ± 0.042	4.014 ± 0.2[a]
f_{C1}, Hz	0.093 ± 0.015	0.133 ± 0.01[b]
f_{C2}, Hz	1.85 ± 0.15	0.92 ± 0.08[a]
L_N, s	0.11 ± 0.003	0.155 ± 0.008[a]
Peak response, %	−2.44 ± 0.44	−11.2 ± 0.5[a]
Time to peak, s	0.19 ± 0.01	0.36 ± 0.02[a]
Peripheral arc		
K_P, mm·%$^{-1}$	0.52 ± 0.07	0.60 ± 0.06
f_{NP}, Hz	0.06 ± 0.01	0.07 ± 0.01
ζ	1.00 ± 0.07	1.06 ± 0.09
L_P, s	0.44 ± 0.02	0.45 ± 0.01
Steady state response, mmHg	0.51 ± 0.06	0.58 ± 0.05
Initial slope, mmHg·%$^{-1}$·s^{-1}	0.049 ± 0.007	0.058 ± 0.005

Data are means ± SE (n = 10 in each group).
[a] $P < 0.001$.
[b] $P < 0.05$.

Estimates of coherence vary between zero and unity. Coherence equal to unity implies perfect linear coupling between input and output signals, whereas a coherence of zero indicates an output that is linearly independent from the input (Bendat and Piersol, 2010). Coherence is lowered by noise components in the output signal unrelated to the input stimulation and nonlinear system responses. The coherence of the A-fiber related central arc transfer function was low between 0.01 and 0.1 Hz, which suggests that the A-fiber central pathway did not contribute much to the SNA variation in these low modulation frequencies. In contrast, the coherence of the C-fiber related central arc transfer function was relatively high at all modulation frequencies, which indicates that the C-fiber central pathway governed the SNA output in the frequency range under study.

A possible mechanism for the observed difference in A- and C-fiber central pathways is neuronal adaptation. Adaptation is generally defined as a decline in response during a maintained stimulus of constant intensity. Adaptation of baroreceptor activity from a sustained elevation in input pressure is dependent on a K^+ current that is blocked by 4-aminopyridine (Chapleau et al., 1993). Baroreceptive second order neurons may also adapt to sustained baroreceptor input in a similar way to the baroreceptor afferents that they are associated with. The C-fiber central pathway may not adapt to the same degree as the A-fiber central

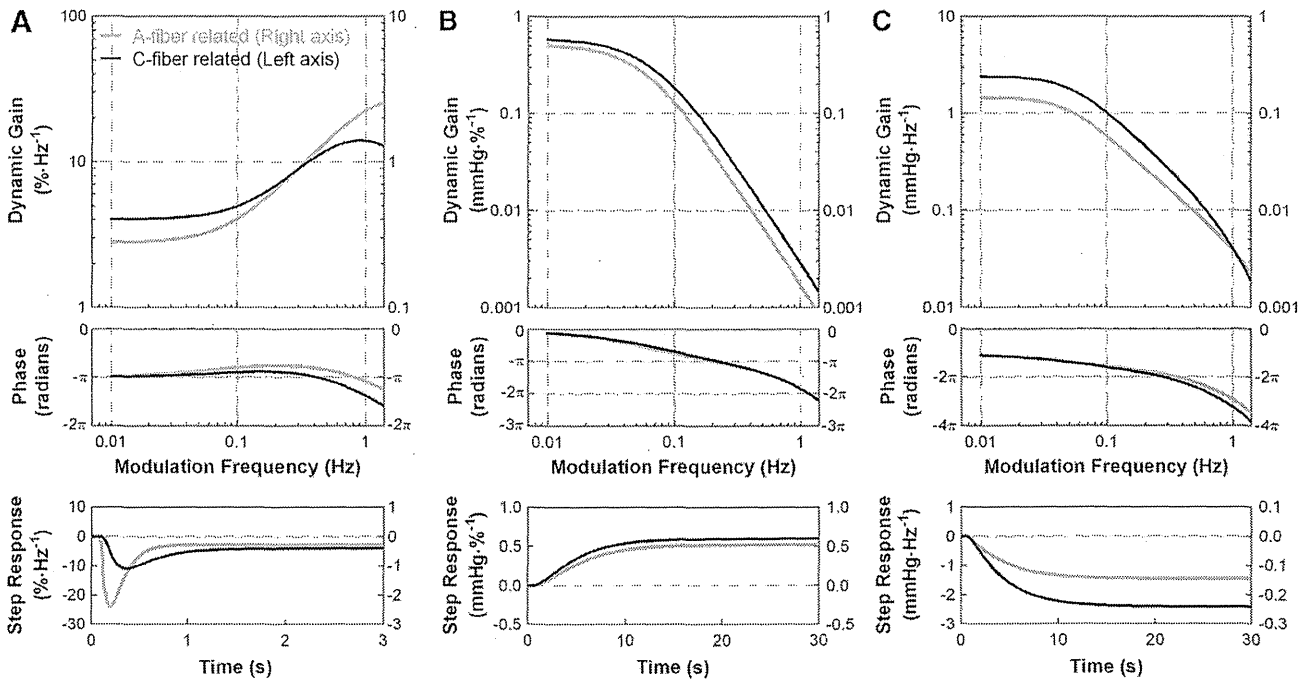

Fig. 6. Simulation of transfer functions and step responses of the central arc (a), peripheral arc (b), and Stim-AP arc (c). In the central arc (a) and Stim-AP arc (c) transfer functions, dynamic gain is displayed in units of output change per stimulation frequency. The ordinate (right axis) for A-fiber related transfer functions (gray lines) in the central arc (a) and Stim-AP arc (c) was shifted upwards by an order of magnitude for relative comparison with C-fiber related transfer functions (black lines). A- and C-fiber related transfer functions and step responses of the Stim-AP arc are the product of the central and peripheral arcs. The majority of the difference in the transfer functions and step responses between A- and C-fiber related responses of the total baroreflex can be attributed to differences in the central arc.

Author's personal copy

pathway over the short-term and only partially reset in the long-term (Jones and Thoren, 1977), which may account for sustained responses observed in the step protocol and dynamic protocol with high-voltage stimulation.

Methodological consideration

Fan and colleagues (Fan and Andresen, 1998; Fan et al., 1999) demonstrated that A-fiber baroreceptors were activated by low intensity (<3 V) stimulation and required minimum frequencies above 10 Hz to evoke reflex reductions in AP. In contrast, high stimulation intensities (20 V) maximally activated both A- and C-fiber baroreceptors, and high intensity stimulation decreased MAP at low frequency (1 Hz) stimulation. Furthermore, the application of capsaicin blocked the reflex response observed at high intensity and low frequency (Fan and Andresen, 1998). Reflex responses at supramaximal intensity during capsaicin were not significantly different from pre-capsaicin low intensity stimulation reflex responses (Fan and Andresen, 1998). Our findings are largely in agreement with the conclusions from Fan and colleagues.

The data from our graded frequency step stimulation protocol added new findings that low intensity stimulation of the ADN resulted in reflex responses that returned towards pre-stimulation levels after only 30 seconds of continuous stimulation. In contrast, high intensity stimulation resulted in sustained reductions in SNA and MAP, but after the application of RTX the responses became similar to those of low intensity stimulation. These data indicate that A-fiber baroreceptors, while being able to account for approximately 70–80% of the combined maximal reflex response to high-frequency stimulation in the study by Fan and Andresen (1998), only contribute to the reflex responses over a short time frame. Activation of C-fiber baroreceptor central pathways appears to be required to elicit reflex responses that are sustained throughout the duration of stimulation.

Based on the results of the step stimulation protocol, LVHf and HVLf dynamic stimulation protocols were devised to chiefly activate reflex response from A- and C-fiber baroreceptors, respectively. Note that although HVLf stimulation can activate both A- and C-fibers, the frequency is considered to be below the physiological threshold for recruiting the A-fiber central pathway (Fan and Andresen, 1998). Our data supports the rationale for selected stimulation protocols, because the central arc transfer functions obtained from LVHf stimulation protocol were largely unaffected by the application of RTX. In contrast, the HVLf stimulation protocol resulted in responses largely from C-fiber type baroreceptors as the application of RTX significantly reduced both dynamic gain and coherence of the central arc transfer functions.

Limitations

While the present study provides insight into how electrical activation of the arterial baroreflex relates to changes in SNA and AP there are some caveats to consider. First, action potential trains from electrical stimulation have a significantly different profile from those evoked by natural pressure stimulation of A- and C-fiber baroreceptors. Secondly, we investigated the responses to electrical stimulation of the ADN in anesthetized rats. Anesthesia may affect SNA, therefore, our results might differ had the experiments been performed in conscious animals. Furthermore, long-term stimulation of either A- or C-fiber baroreceptors is required to conclude that sustained reductions are mediated via C-fiber baroreceptor central pathways. However, given the very small involvement of A-fiber baroreceptor central pathways to the reduction of SNA after only 30 seconds and limited reduction in both SNA and AP during the 20 minute LVHf binary white noise stimulation protocol, it appears unlikely that A-fiber stimulation would be able to reduce SNA chronically. Examining electrical stimulation of A- and C-fiber baroreceptors in animal models of hypertension may be a possible future direction of study. Lastly, we also sectioned vagi to remove the influences of cardiopulmonary reflexes on SNA thus opening the arterial baroreflex negative feedback loop. Consequently, the transfer function of the Stim-AP arc does not include the vagal limb of the baroreflex. Further investigation is required to identify how selective stimulation of A- and C-fiber baroreceptors affects the vagal limb of the arterial baroreflex.

Conclusion

While device-based therapies that activate the arterial baroreflex have shown promising reductions in AP in resistant-hypertension patients the central pathways involved are still not entirely understood. This study highlights the two distinct baroreceptor pathways that need to be considered when investigating the role of the arterial baroreflex in the regulation of AP in health and disease. Furthermore, it indicates that electrical stimulation of C-fiber baroreceptors may be integral for a sustained reduction in AP, which is consistent with an increasingly large body of evidence that the arterial baroreflex can chronically inhibit SNA (Thrasher, 2005b; Lohmeier and Iliescu, 2011). A greater understanding of the integration and processing of the arterial baroreflex may also lead to novel ways of directly targeting either A- or C-fiber baroreceptor central pathways to chronically lower SNA and AP in hypertensive patients.

Grants

This study was supported by Health and Labour Sciences Research Grants (H19-nano-Ippan-009, H20-katsudo-Shitei-007, and H21-nano-Ippan-005) from the Ministry of Health, Labour and Welfare of Japan; Intramural Research Fund (25-6-17) of the National Cerebral and Cardiovascular Center; Grant-in-Aid for Scientific Research (JSPS KAKENHI Grant Number 23592319); and Grant-in-Aid for JSPS Fellows (JSPS KAKENHI Grant Number 2301705).

Conflict of interest

The authors declared no conflict of interest.

References

Bakris GL, Nadim MK, Haller H, Lovett EG, Schafer JE, Bisognano JD. Baroreflex activation therapy provides durable benefit in patients with resistant hypertension: results of long-term follow-up in the Rheos Pivotal Trial. J Am Soc Hypertens 2012;6:152–8.
Bendat JS, Piersol AG. Random data: analysis and measurement procedures. New Jersey: Wiley, Hoboken; 2010.
Brown AM, Saum WR, Yasui S. Baroreceptor dynamics and their relationship to afferent fiber type and hypertension. Circ Res 1978;42:694–702.
Chapleau MW, Lu J, Hajduczok G, Abboud FM. Mechanisms of baroreceptor adaptation in dogs: attenuation of adaptation by the K+ channel blocker 4-aminopyridine. J Physiol 1993;462:291–306.
Cowley Jr AW. Long-term control of arterial pressure. Physiol Rev 1992;72:231–300.
Fan W, Andresen MC. Differential frequency-dependent reflex integration of myelinated and nonmyelinated rat aortic baroreceptors. Am J Physiol Heart Circ Physiol 1998; 275:632–40.
Fan W, Schild JH, Andresen MC. Graded and dynamic reflex summation of myelinated and unmyelinated rat aortic baroreceptors. Am J Physiol Regul Integr Comp Physiol 1999; 277:748–56.
Fazan VP, Salgado HC, Barreira AA. Aortic depressor nerve unmyelinated fibers in spontaneously hypertensive rats. Am J Physiol Heart Circ 2001;4:1560–4.
Guyton AC. Arterial pressure and hypertension. Philadelphia, PA: Saunders; 1980.
Jones JV, Thoren PN. Characteristics of aortic baroreceptors with nonmedullated afferents arising from the aortic arch of rabbits with chronic renovascular hypertension. Acta Physiol Scand 1977;101:286–93.
Kawada T, Zheng C, Yanagiya Y, Uemura K, Miyamoto T, Inagaki M, Shishido T, Sugimachi M, Sunagawa K. High-cut characteristics of the baroreflex neural arc preserve baroreflex gain against pulsatile pressure. Am J Physiol Heart Circ Physiol 2002;282:1149–56.
Kawada T, Shimizu S, Kamiya A, Sata Y, Uemura K, Sugimachi M. Dynamic characteristics of baroreflex neural and peripheral arcs are preserved in spontaneously hypertensive rats. Am J Physiol Regul Integr Comp Physiol 2010;300:155–65.
Krieger EM. Neurogenic mechanisms in hypertension: resetting of the baroreceptors. Hypertension 1986;8:7–14.
Kubo T, Imaizumi T, Harasawa Y, Ando S, Tagawa T, Endo T, Shiramoto M, Takeshita A. Transfer function analysis of central arc of aortic baroreceptor reflex in rabbits. Am J Physiol Heart Circ Physiol 1996;39:1054–62.

Author's personal copy

Lohmeier TE, Iliescu R. Chronic lowering of blood pressure by carotid baroreflex activation: mechanisms and potential for hypertension therapy. Hypertension 2011;57:880–6.
Lohmeier TE, Iliescu R, Liu B, Henegar JR, Maric-Bilkan C, Irwin ED. Systemic and renal-specific sympathoinhibition in obesity hypertension. Hypertension 2012;59:331–8.
Numao Y, Siato M, Terui N, Kumada M. The aortic nerve-sympathetic reflex in the rat. J Auton Nerv Syst 1985;13:65–79.
Petiot E, Barrès C, Chapuis B, Julien C. Frequency response of renal sympathetic nervous activity to aortic depressor nerve stimulation in the anaesthetized rat. J Physiol 2001;537:949–59.
Reynolds PJ, Fan W, Andresen MC. Capsaicin-resistant arterial baroreceptors. J Negat Results Biomed 2006;5:6–15.
Stocker SD, Muntzel MS. Recording sympathetic nerve activity chronically in rats: surgery techniques, assessment of nerve activity, and quantification. Am J Physiol Heart Circ Physiol 2013;305:H1407–16.
Sun H, Li D, Chen S, Hittelman WN, Pan H. Sensing of blood pressure increase by transient receptor potential vanilloid 1 receptors on baroreceptors. J Pharmacol Exp Ther 2009;331:851–9.
Thoren P, Munch PA, Brown AM. Mechanisms for activation of aortic baroreceptor C-fibres in rabbits and rats. Acta Physiol Scand 1999;166:167–74.
Thrasher TN. Baroreceptors, baroreceptor unloading, and the long-term control of blood pressure. Am J Physiol Integr Comp Physiol 2005a;288:819–27.
Thrasher TN. Effects of chronic baroreceptor unloading on blood pressure in the dog. Am J Physiol Regul Integr Comp Physiol 2005b;288:863–71.